RUNX1 marks a luminal castration resistant lineage established at the onset of prostate development

AUTHORS

Renaud Mevel[1], Ivana Steiner[2], Susan Mason[3], Laura Galbraith[3], Rahima Patel[1], Muhammad ZH Fadlullah[1], Imran Ahmad[3,4], Hing Y. Leung[3,4], Pedro Oliveira[5], Karen Blyth[3,4], Esther Baena[2,6], Georges Lacaud[1,7]

AFFILIATIONS

[1] Cancer Research UK, Stem Cell Biology Group, Cancer Research UK Manchester Institute, The University of Manchester, Alderley Park, Alderley Edge, Macclesfield, SK10 4TG, UK.

[2] Cancer Research UK, Prostate Oncobiology Group, Cancer Research UK Manchester Institute, The University of Manchester, Alderley Park, Alderley Edge, Macclesfield, SK10 4TG, UK.

[3] Cancer Research UK Beatson Institute, Bearsden, Glasgow, G61 1BD, UK.

[4] Institute of Cancer Sciences, College of Medical, Veterinary and Life Sciences, University of Glasgow, Bearsden, Glasgow, G61 1QH, UK.

[5] Department of Pathology, The Christie NHS Foundation Trust, Manchester, UK.

[6] Belfast-Manchester Movember Centre of Excellence, Cancer Research UK Manchester Institute, The University of Manchester, Alderley Park SK10 4TG, UK.

[7] Correspondence: georges.lacaud@manchester.ac.uk

Phone: +44 (0) 161 446 6058, Fax: +44 (0) 161 446 3109

ABSTRACT

The development of castration-resistant prostate cancer is a major complication of androgen-deprivation therapy. However, the origin and identity of these resistant cells remains controversial. Here, we report that the transcription factor RUNX1 marks a specific subpopulation of proximal luminal cells (PLCs), enriched in the periurethral region of the developing and adult mouse prostate, and distinct from the previously identified NKX3.1^{+} luminal castration resistant cells. Using scRNA-seq profiling and genetic lineage tracing, we show that RUNX1^{+} PLCs are unaffected by androgen deprivation, and do not contribute to the regeneration of the distal luminal compartments. Furthermore, we demonstrate that a transcriptionally similar RUNX1^{+} population emerges at the onset of embryonic prostate specification to populate the proximal region of the ducts. Collectively, our results reveal that RUNX1^{+} PLCs is an intrinsic castration-resistant and self-sustained lineage that emerges early during prostate development and provide new insights into the lineage relationships of the prostate epithelium.

34 **INTRODUCTION**

35 Prostate is a glandular organ of the mammalian male reproductive system and Prostate
36 Cancer (PCa) is the most frequently diagnosed cancer in men. One limitation in its treatment is
37 the difficulty to accurately discriminate between indolent and more aggressive forms of the
38 disease. Therefore, a greater understanding of PCa, as well as normal prostate biology would be
39 transformative in improving current diagnostic and treatment modalities.

40 In mice, prostate development starts during embryogenesis at embryonic day (E) 15.5-
41 16.5 with the emergence of the first prostatic buds from the rostral end of the urogenital sinus
42 (UGS) (Bhatia-Gaur et al., 1999; Georgas et al., 2015; Keil et al., 2012; Toivanen & Shen, 2017).
43 These initial buds grow into the surrounding mesenchyme to develop postnatally and through
44 puberty into a branched ductal network organized in distinct pairs of lobes, known as the
45 anterior prostate (AP), dorsolateral prostate (DLP) and ventral prostate (VP) (Sugimura et al.,
46 1986a). Each lobe has distinct branching patterns, histopathological characteristics, and is
47 thought to contribute differently to the physiological function of the prostate. The
48 differentiated epithelium of the adult prostate gland is mainly composed of basal and luminal
49 cells, interspersed with rare neuroendocrine cells (Shen & Abate-Shen, 2010; Toivanen & Shen,
50 2017; Y. Wang et al., 2001). Luminal cells form a layer of polarized tall columnar cells that
51 depend on androgen signaling and produce the prostatic secretions. Basal cells act as a
52 supportive layer located between the luminal cells and the surrounding stroma.

53 In PCa patients, androgen deprivation therapy (ADT) is frequently used to target
54 androgen-dependent tumor cells. However, the emergence of castration-resistant PCa cells,
55 proposed to either originate from intrinsically castration-resistant subpopulations or to be

56 acquired *de novo*, is a major limitation of this treatment (Shen & Abate-Shen, 2010; Zhang et
57 al., 2018). Therefore, understanding the origin and identity of these resistant cells both in the
58 normal prostate and PCa represents an essential step towards improving PCa treatments. In
59 mice, surgical castration-induced prostate involution has proven an invaluable tool to identify
60 progenitor castration-resistant cell populations, characterized by their ability to survive in the
61 absence of androgens, and to fully regenerate an intact adult prostate after re-administration
62 of testosterone (Barros-Silva et al., 2018; Kwon et al., 2016; McAuley et al., 2019; Tsujimura et
63 al., 2002; B. Wang et al., 2015; X. Wang et al., 2009; Yoo et al., 2016). Indeed, despite being
64 mostly quiescent under homeostatic conditions, the prostate gland encompasses incredible
65 plasticity. Such plasticity has also been shown in defined experimental conditions to stimulate
66 regenerative properties of epithelial subpopulations, including transplantations (Barros-Silva et
67 al., 2018; Burger et al., 2005; Lawson et al., 2007; Lukacs et al., 2010; Richardson et al., 2004; X.
68 Wang et al., 2009; Xin et al., 2005; Yoo et al., 2016), injury repair (Horton et al., 2019; Kwon et
69 al., 2014; Toivanen et al., 2016), and organoid assays (Chua et al., 2014; Höfner et al., 2015;
70 Karthaus et al., 2014). In addition, several studies have proposed that progenitor populations
71 with distinct physiological roles and regenerative capacity reside at different locations within
72 the prostate (Burger et al., 2005; Crowell et al., 2019; Goldstein et al., 2008; Goto et al., 2006;
73 Kwon et al., 2016; Leong et al., 2008; McNeal, 1981; Tsujimura et al., 2002). However, the
74 precise cellular hierarchy and how it is established during development remains controversial.
75 RUNX transcription factors (TF) are master regulators of lineage commitment and cell
76 fate (Mevel et al., 2019). In particular, RUNX1 is essential for the ontogeny of the hematopoietic
77 system and alterations of RUNX1 have been associated with a broad spectrum of hematological

78 malignancies. Interestingly, increasing evidence implicates RUNX1 in the biology and pathology
79 of hormone-associated epithelia (Lie-A-Ling et al., 2020; Riggio & Blyth, 2017; Scheitz &
80 Tumbar, 2013), including breast (Browne et al., 2015; Chimge et al., 2016; Ferrari et al., 2014;
81 van Bragt et al., 2014), uterine (Planagumà et al., 2004, 2006), ovarian (Keita et al., 2013), and
82 prostate cancers (Banach-Petrosky et al., 2007; Scheitz et al., 2012; Takayama et al., 2015).
83 Despite the documented importance of RUNX TFs and reports of RUNX1 in PCa, its expression
84 in the normal prostate gland during development, homeostasis, and regeneration has not been
85 explored.

86 In this study, we found that *Runx1* marks a discrete subset of luminal cells located in the
87 proximal region of the prostatic ducts. Using mouse models, combined with lobe-specific single-
88 cell transcriptomic profiling of adult, castrated, and developing prostates, we show that RUNX1^{+}
89 proximal luminal cells represent a distinct lineage established at the onset of prostate
90 development, displaying intrinsic castration-resistant and self-sustaining properties.

91 **RESULTS**

92 **RUNX1 marks a subpopulation of prostate proximal luminal cells (PLCs)**

93 We initially sought to characterize the expression pattern of *Runx1* in adult mouse
94 prostate. While RUNX1 was detected in basal cells at multiple spatial locations, its expression
95 was specifically high in a subset of luminal cells found in the proximal region of all three lobes,
96 also known as periurethral (Figures 1A, B; Figure 1–figure supplement 1A, B). Sections were co-
97 stained with NKX3.1, a master regulator of prostate development broadly expressed in luminal
98 cells. Using quantitative image-based cytometry (QBIC), we found that RUNX1 and NKX3.1 had
99 a largely mutually exclusive expression pattern, with a sharp transition from RUNX1^{+} NKX3.1^{-} to
100 RUNX1^{-} NKX3.1^{+} cells in the proximal region (Figures 1A, B; Figure 1–figure supplement 1A, B).
101 These proximal luminal cells had a unique histological profile, with a compact organization,
102 intense nuclear hematoxylin staining, and increased nuclear-to-cytoplasmic ratio (Figure 1–
103 figure supplement 1C). In contrast, distal luminal cells had a large cytoplasm with intense pink
104 eosin staining, likely reflecting their secretory function. These observations suggest that RUNX1
105 marks a subset of proximal luminal cells, distinct from the abundant NKX3.1^{+} luminal population
106 lining the rest of the prostate epithelium.

107 The proximal site of the prostate has been proposed to be enriched in cells with
108 stem/progenitor properties (Goldstein et al., 2008; Kwon et al., 2016; Tsujimura et al., 2002;
109 Yoo et al., 2016). In order to study the regenerative potential of *Runx1* expressing cells *ex vivo*,
110 we took advantage of isoform-specific fluorescent reporter mouse models of *Runx1* (Draper et
111 al., 2018; Sroczynska et al., 2009). *Runx1* expression is controlled by two promoters, P1 and P2,
112 that respectively drive the expression of the *Runx1c* and the *Runx1b* isoform (Mevel et al.,

113 2019). We found that *Runx1* expression in the prostate was exclusively mediated by the
114 proximal P2 promoter, in up to 30% of all epithelial EPCAM$^+$ prostate cells (Figures 2A-C). Flow-
115 cytometry profiling confirmed the enrichment of P2-*Runx1*:RFP in both basal (EPCAM$^+$
116 CD49f^{high}) and luminal (EPCAM$^+$ CD24^{high}) lineages of the proximal compared to the distal
117 prostate (Figures 1C, D; Figure 1–figure supplement 2D). Mirroring our QBIC spatial analysis
118 (Figure 1–figure supplement 1B), P2-*Runx1*:RFP was also detected in a large fraction of the VP
119 epithelium (Figure 1–figure supplement 2D).
120 We therefore used the P2-*Runx1*:RFP mouse line to isolate *Runx1* positive (RFP$^+$) and
121 negative (RFP$^-$) epithelial cells from the basal and luminal compartments of all three prostate
122 lobes and evaluated their regenerative potential in organoid culture assays (Drost et al., 2016)
123 (Figure 1E). The proximal and distal regions of the AP were analysed separately. Proximal RFP$^+$
124 luminal cells of the AP consistently displayed higher Organoid Formation Capacity (OFC) than
125 the RFP$^-$ fraction (Figure 1F). Luminal RFP$^+$ sorted cells of the DLP and VP also had a greater OFC
126 than RFP$^-$ cells (Figure 1–figure supplement 3A). In contrast, no significant differences in OFC
127 were observed between basal enriched subsets and distal luminal RFP$^+$ and RFP$^-$ cells.
128 Brightfield assessment revealed that virtually all organoids had a 'solid' aspect, except for the
129 predominantly 'hollow' organoids derived from proximal RFP$^+$ luminal cells (Figure 1–figure
130 supplement 3B). To further characterize their lineage potential, we classified organoids into
131 three types based on the expression of specific lineage markers: unipotent "basal-like" Keratin
132 5$^+$ (K5$^+$), unipotent "luminal-like" Keratin 8$^+$ (K8$^+$), or multipotent K5$^+$ K8$^+$ (Figures 1G, H; Figure
133 1–figure supplement 3C). Interestingly, AP proximal luminal RFP$^+$ derived organoids were
134 predominantly small unipotent K8$^+$, while the remainder fraction mainly gave larger unipotent

135 K5$^+$ organoids (Figures 1H; Figure 1–figure supplement 3D). Few multipotent K5$^+$ K8$^+$ organoids
136 were also identified in nearly all populations.
137 Together, our results show that RUNX1 marks a specific subset of proximal luminal cells
138 (PLCs), and that its expression in the prostate is mediated by the P2 promoter. RUNX1$^+$ PLCs
139 have a particular predisposition to form unipotent K8$^+$ hollow organoids, suggesting a lineage
140 bias towards the luminal identity, and highlighting differences within the luminal compartment
141 of proximal and distal regions.
142
143 ***Runx1* expressing cells are enriched in the castrated prostate epithelium**
144 In mice, androgen-deprivation can be modelled by surgical castration which leads to
145 prostate regression and enriches for castration-resistant cells (Toivanen & Shen, 2017; Zhang et
146 al., 2018). This process is accompanied by the death of luminal androgen-dependent cells and a
147 small proportion of basal cells (English et al., 1987; Sugimura et al., 1986b). To track changes in
148 *Runx1* expression following androgen withdrawal, we surgically castrated P2-*Runx1*:RFP mice
149 and harvested tissue ≥ 4 weeks post-surgery (Figure 2A). While intact prostates contained 22.8
150 ± 6.0% RFP$^+$ epithelial cells, their frequency increased to 87 ± 6.0% following castration (Figures
151 2B, C). High RUNX1 levels were no longer restricted to the proximal region, and RFP was
152 detected in virtually all basal cells of the AP, DLP and VP, as well as more than 75% of the
153 luminal castration-resistant cells (Figures 2D; Figure 2–figure supplement 4A). RUNX1
154 expressing cells often co-expressed TROP2 (Figure 2E), known to be widely expressed in
155 castrated prostate epithelium (Goldstein et al., 2008; X.-D. Wang et al., 2007). Several
156 castration-resistant luminal populations have been identified in mice (Barros-Silva et al., 2018;

157 Kwon et al., 2016; McAuley et al., 2019; Tsujimura et al., 2002; B. Wang et al., 2015; X. Wang et
158 al., 2009; Yoo et al., 2016), including rare castration-resistant *Nkx3-1* expressing cells (CARNs).
159 Accordingly, we observed low, but detectable, levels of NKX3.1 in some luminal cells, but only
160 occasional RUNX1$^+$ NKX3.1$^+$ luminal cells in the distal regions of the castrated prostate (Figures
161 2D; Figure 2–figure supplement 4B, C). Importantly, the clear transition from RUNX1$^+$ to
162 NKX3.1$^+$ cells identified in the proximal luminal layer of intact mice was conserved after
163 castration (Figure 2D, ii).
164 Together, these results show that RUNX1 is expressed in the majority of the castration-
165 resistant cells. The RUNX1$^+$ NKX3.1$^-$ subset identified in the proximal luminal epithelium of the
166 intact prostate remain NKX3.1$^-$ following castration, supporting the notion that RUNX1$^+$ PLCs
167 constitute a distinct lineage from distal NKX3.1$^+$ cells.
168
169 **scRNA-seq profiling of *Runx1*$^+$ and *Runx1*$^-$ cells in individual lobes of the intact and castrated**
170 **prostate**
171 To further characterize the RUNX1$^+$ and RUNX1$^-$ fractions residing at different
172 anatomical locations of the prostate, we performed droplet-based single cell (sc)RNA-seq. We
173 sorted EPCAM$^+$ RFP$^+$ and RFP$^-$ cells from individually dissected lobes of intact and castrated
174 prostates isolated from P2-*Runx1*:RFP reporter mice (Figure 3A). Sorted populations were
175 multiplexed using MULTI-seq lipid-tagged indices to minimize technical confounders such as
176 doublets and batch effects (McGinnis et al., 2019). We retrieved a total of 3,825 prostate
177 epithelial cells from all sorted populations, with a median of 2,846 genes per cell (see Methods;
178 Figure 3–figure supplement 5, 6A-G). We identified 9 *in silico* computed clusters expressing

179 canonical epithelial, basal, and luminal markers (Figure 3–figure supplement 6H-J). A large
180 population of basal cells was annotated by merging 3 tightly connected subclusters broadly
181 expressing *Krt5*, *Krt14,* and *Trp63* (Figures 3B-D; Figure 3–figure supplement 6E, J). Luminal
182 populations expressed surprisingly heterogeneous levels of canonical luminal markers such as
183 *Cd26*/*Dpp4, Cd24a*, *Krt8, and Krt18* (Figure 3–figure supplement 6I). We annotated those
184 distinct clusters as Luminal-A (Lum-A), Lum-B, Lum-C, Lum-D, Lum-E and Lum-F (Figure 3B).
185 Differential gene expression analysis revealed genes strongly associated with each luminal
186 subpopulation (Figures 3C, 3D; Figure 3–figure supplement 7A; Supplementary file 2).
187 Initially, we sought to evaluate the effect of androgen withdrawal on lobe-specific
188 cellular heterogeneity. Lum-A/B/C/D were largely enriched in luminal cells originating from
189 intact prostates, whereas Lum-E/F contained mainly castrated luminal cells (Figures 3E; Figure
190 3–figure supplement 7B). However, a small fraction of intact cells was also identified in Lum-
191 E/F, while some castrated cells were found in Lum-A/B/C/D clusters. Interestingly, Lum-A/C/F
192 mainly contained VP cells, while Lum-B/D/E had a majority of AP and DLP cells, indicating that
193 the lobular identity of luminal cells in the intact prostate is conserved following castration
194 (Figures 3F; Figure 3–figure supplement 7C). This suggests that a subset of intact Lum-A/C
195 undergoes partial reprogramming during castration-induced regression and gives rise to the
196 Lum-F cluster. Similarly, surviving Lum-B/D may predominantly reprogram into Lum-E cells
197 upon castration. In contrast, castrated basal cells were minimally affected by androgen-
198 deprivation and clustered together with intact basal cells (Figure 3E). Overall, our dataset
199 highlights the broad transcriptional reprogramming occurring predominantly in luminal cells
200 upon androgen deprivation.

201

202 ***Runx1* expressing luminal cells are transcriptionally similar to castration-resistant cells**

203 We next specifically focused our attention on RUNX1$^+$ luminal cells. The Lum-D cluster
204 predominantly consisted of AP derived RFP$^+$ cells, as well as a small number of RFP$^+$ DLP and VP
205 cells (Figure 3F, H; Figure 3–figure supplements 6E, 7B, 7C). High *Runx1* expression in Lum-D
206 correlated with higher levels of *Tacstd2*/*Trop2*, Ly6 family members as well as *Runx2* (Figures
207 3D, G; Figure 3–figure supplements 7D, E). In contrast, *Runx1* was barely detected in clusters
208 Lum-B/C which expressed high levels of *Nkx3-1* while Lum-A cells expressed low levels of both
209 *Runx1* and *Nkx3-1*. These results suggest that the Lum-D cluster corresponds to the distinct
210 RUNX1$^+$ luminal cells identified in the proximal region of all three prostate lobes (Figure 1).

211 To further characterize the specificities of those populations, we performed gene
212 ontology analysis. In line with the secretory role of distal luminal cells, clusters Lum-A/B/C were
213 enriched in enzymatic activity and protein synthesis functions. In contrast, the Lum-D cluster
214 was enriched in terms related to epithelial developmental processes, similar to Lum-E/F (Figure
215 3–figure supplements 8A-I). This was supported by partition-based graph abstraction (Wolf et
216 al., 2019), which uncovered a strong degree of connectivity between the mainly intact Lum-D
217 and castrated Lum-E population (Figure 3B). Additionally, the Lum-D cluster contained a small,
218 but defined, subpopulation of castrated epithelial cells, suggesting the preservation of its
219 identity upon androgen deprivation (Figures 3E, F). In this population, we found very few genes
220 significantly differentially expressed between intact and castrated cells (n=103; Supplementary
221 file 3). As expected, androgen-regulated genes including *Psca* and *Tspan1* were downregulated
222 in the castrated subset, while strong contributors of the Lum-D identity such as *Tacstd2*/*Trop2*,

223 *Krt4* and *Runx1* did not vary (Figure 3–figure supplement 8J). These observations further
224 support the hypothesis that Lum-D/RUNX1^{+} PLCs maintain their identity following androgen-
225 deprivation.
226 Overall, our single-cell transcriptomic analysis highlighted a vast degree of
227 heterogeneity within and between the luminal compartments of both intact and castrated
228 mouse prostates. The tight transcriptional relationship observed between high *Runx1*
229 expressing clusters Lum-D and Lum-E/F suggest that the Lum-D population, which corresponds
230 to PLCs, may contain intrinsically castration-resistant luminal cells
231
232 **Lineage-tracing of *Runx1* expressing cells establishes the intrinsic castration resistant**
233 **properties of the proximal luminal lineage**
234 To determine if RUNX1^{+} PLCs were enriched in castration-resistant cells, we combined
235 prostate regression-regeneration assays with genetic lineage-tracing using *Runx1*$^{mER\text{-}CRE\text{-}}$
236 ^{mER}*Rosa*$^{Flox\text{-}stop\text{-}Flox\text{-}RFP}$ mice (Luche et al., 2007; Samokhvalov et al., 2007), henceforth *Runx1*$^{CRE\text{-}}$
237 $^{stop\text{-}RFP}$ (Figure 4A). Using this model, we could genetically label an average of 4.70 ± 2.8%
238 prostate epithelial *Runx1* expressing cells with RFP upon tamoxifen injection (Figures 4B, C;
239 Figure 4–figure supplement 9A). This corresponded to 0.54 ± 0.2‰ of the total epithelium
240 (Figure 4E). Consistent with the expression pattern of *Runx1*, the majority of labelled cells were
241 located in the proximal region of the prostate (Figure 4C), and co-expressed Keratin 4 (K4)
242 (Figure 4–figure supplements 9D, E), previously found enriched in Lum-D cells (Figure 3D).
243 Following surgical castration, we found that the absolute number of RFP^{+} marked cells
244 remained stable (Figure 4–figure supplements 9C, D). However, the frequency of RFP^{+} cells in

245 the epithelial compartment increased by ~4.3 fold (Figures 4E; Figure 4–figure supplement 9B)
246 indicating that *Runx1* expressing cells have an enhanced capacity to survive castration
247 compared to *Runx1* negative cells. Next, we investigated whether these intrinsically castration-
248 resistant *Runx1* expressing cells were involved in epithelial regeneration upon testosterone
249 addback (Figure 4B, bottom). Surprisingly, only 0.71 ± 0.2‰ RFP^+ epithelial cells were found in
250 the regenerated prostate, which was comparable to the intact state (Figures 4E; Figure 4–figure
251 supplements 9B-D). Although the majority of RFP^+ clones consisted of single cells, we did
252 observe a minor ~2-fold increase in the frequency of larger clones (2-4 cells) after regeneration,
253 highlighting a modest contribution of RFP labeled cells during prostate regeneration (Figures 4F,
254 G). We found that most RFP marked cells were luminal $K8^+$ in intact, castrated, and regenerated
255 prostates (Figures 4F, H), with only a few basal $K5^+$ RFP^+ cells detected in distal areas (Figure
256 4F). Strikingly, more than 90% of all RFP^+ cells remained negative for NKX3.1 in all experimental
257 arms (Figure 4I).
258 Thus, these results indicate that RFP^+ cells, including PLCs, are mostly unaffected by
259 fluctuations in androgen levels during regression-regeneration assays. RUNX1 expression marks
260 intrinsically castration-resistant luminal cells that do not contribute to the expansion of luminal
261 $NKX3.1^+$ cells during prostate regeneration.
262
263 ***Runx1* marks proximal cells during prostate development**
264 Given the singular identity of proximal luminal *Runx1* expressing cells in the adult
265 prostate, we then asked if this luminal lineage was already emerging during prostate
266 development. At E18.5, once the first prostate buds have emerged, RUNX1 was mainly found in

267 the K8^{high} inner layers of the stratified urogenital epithelium (UGE) (Figure 5A). Interestingly,
268 these cells also co-expressed K4 (Figure 5–figure supplement 10A), previously found in the Lum
269 D population (Figure 3D), as well as LY6D, recently shown to mark a subset of adult luminal
270 progenitors (Barros-Silva et al., 2018) (Figure 5–figure supplement 10B). In contrast, RUNX1
271 expression was low in p63^{+} and K5^{+} cells, either lining the outer UGE or found in the tips of
272 premature NKX3.1^{+} prostate buds (Figures 5A-C). At postnatal day 14 (P14), a prepubescent
273 stage when most of the initial branching events have already occurred (Sugimura et al., 1986a;
274 Tika et al., 2019), RUNX1 was broadly expressed in the proximal region (Figure 5D), mainly in
275 K4^{+} luminal cells and in some K5^{+} or p63^{+} cells (Figure 5–figure supplement 10C-E). Conversely,
276 NKX3.1^{+} cells were found in distal locations, largely distinct from RUNX1^{+} cells. The specific
277 spatial expression pattern of RUNX1 in proximal luminal cells, largely mutually exclusive with
278 NKX3.1, suggests that these two transcription factors already mark distinct cellular lineages
279 during embryonic prostate organogenesis.
280 To study the dynamic emergence of RUNX1^{+} cells during prostate development, we
281 utilized an explant culture system (Berman et al., 2004; Doles et al., 2005; Kruithof-de Julio et
282 al., 2013; Lopes et al., 1996). Dissected E15.5 UGS were cultured for up to 7 days in the
283 presence of dihydrotestosterone (Figures 5E, F). Bud formation was initiated within 2 days of
284 culture (Figure 5G) and composed of a double positive K5^{+} K8^{+} stratified epithelium, partially
285 diversifying by day 7 (Figure 5–figure supplement 11A, B). On day 0 (E15.5), RUNX1 was
286 detected at the rostral end of the UGE, particularly within the inner layers of the stratified
287 epithelium. After 1 day in culture, NKX3.1 expression emerged in RUNX1^{+} cells located in the
288 outer layers of the UGE, while defined budding was yet to be observed. On day 2, NKX3.1^{+}

289 prostate buds were evident and had reduced or absent RUNX1 expression. This pattern was
290 conserved in the mature explant, in which distal tips were mainly NKX3.1$^+$, whereas the
291 proximal area remained RUNX1$^+$ (Figures 5G, H), and co-expressed LY6D and K4 (Figure 5–figure
292 supplements 10C, D). Cellular proliferation marked by Ki67 was more substantial in distal
293 regions, suggesting that most of the expansion did not take place in the RUNX1$^+$ compartment
294 (Figure 5–figure supplement 10E).
295 These results suggest that prostate budding originates from a subset of cells located in
296 the outer layers of the stratified UGE, transiently marked by RUNX1 and NKX3.1. During
297 embryonic prostate development, *Runx1* expression is already primarily confined to the
298 proximal region of the prostatic ducts, in a distinct compartment from NKX3.1$^+$ cells.
299
300 **scRNA-seq of explant cultures reveals the specification of the proximal luminal lineage during**
301 **embryonic prostate development**
302 The characterization by immunostainings of continuous developmental processes is
303 generally constrained to a small number of markers at a time. To further study the specification
304 of RUNX1 and NKX3.1 lineages, we performed scRNA-seq on UGS explant cultures collected at
305 successive time points: E15.5 (D0), day 1 (D1), day 3 (D3), and day 6 (D6) (Figure 6A). After data
306 processing, 3,937 developing prostatic cells were retained, with a median of 3,608 genes per
307 cell (see Methods; Figure 6–figure supplement 12).
308 Visualization of the dataset using a force-directed layout highlighted the progressive
309 cellular diversification taking place from D0 to D6 (Figure 6B). Cellular populations were divided
310 into 9 clusters, annotated C0 to C8 (Figures 6C-E). C0/C1 contained the majority of D0 and D1

311 derived cells, while C2-C8 emerged and expanded at later time points. Due to the primitive
312 nature of the UGE at these time points, the classical basal and luminal lineages were not fully
313 established yet (Figures 6F; Figure 6–figure supplements 13A-E; Supplementary file 4).
314 Nevertheless, C4-C6 had a more pronounced 'basal' identity compared to the other clusters.
315 *Krt5*/*Krt14* marked mainly C4, and additional basal markers including *Trp63, Dcn*, *Apoe,* or *Vcan*
316 were higher in C5/C6. Overall, known regulators of prostate development (Toivanen & Shen,
317 2017) displayed a variable expression pattern across the different clusters. For example, *Foxa1*
318 and *Shh* were strongly expressed in C0/C1, *Notch1* was higher in C3, and *Sox9* in C7 (Figure 6–
319 figure supplement 13C), highlighting the potential of this dataset to interrogate specific
320 features of prostate development.

321 Consistent with our previous results, *Runx1* was highly expressed in clusters having
322 lower *Nkx3-1* levels, including C0, C1, C2 and C4 (Figure 6G). To determine how these clusters
323 relate to differentiated prostate lineages, we interrogated population-specific gene signatures
324 previously identified in the adult (Figure 3). The 'Basal' signature was enriched across all
325 clusters, especially in C4/C6 (Figures 6I; Figure 6–figure supplement 13F, G). Strikingly, the
326 'Lum-D' derived signature was highly enriched in C2 compared to all the other adult luminal
327 population signatures, suggesting that the 'Lum-D' fate is determined early during prostate
328 development. The singular identity of C2 was characterized by genes previously found highly
329 expressed in the adult 'Lum-D' population, including *Tacstd2*/*Trop2*, *Krt4*, *Psca*, as well as *Ly6d*
330 and *Nupr1* (Figure 6H; Figure 6–figure supplement 13A).

331 Collectively, our scRNA-seq analysis show that adult 'Lum-D'/PLCs share strong
332 similarities with the unique C2 population identified in embryonic explant cultures. This

333 suggests that the distinct proximal luminal lineage is established at the very onset of prostate
334 specification.
335
336 **RUNX1$^+$ cells contribute to the establishment of the proximal luminal lineage during**
337 **embryonic prostate development**
338 To trace the fate of RUNX1$^+$ cells during embryonic prostate specification, we cultured
339 UGS explants isolated from the *Runx1*$^{CRE\text{-}stop\text{-}RFP}$ lineage tracing model. We performed 2 pulses
340 of tamoxifen treatment on day 0 and 1 of culture and analyzed the explants on day 2 and day 7
341 (Figure 7A). The majority of the RFP labeled cells were in the most proximal RUNX1$^+$ subset and
342 rarely found in the distal area of the branches, where RUNX1$^-$ cells reside (Figures 7B, C).
343 Accordingly, the proportion of RFP$^+$ RUNX1$^+$ cells remained stable between day 2 and 7 (Figure
344 7D). Also, the fraction of RFP$^+$ cells co-expressing p63 remained unchanged throughout the
345 culture (Figure 7–figure supplements 14A-C), while a small fraction diversified into either K5$^+$ or
346 K8$^+$ cells (Figure 7–figure supplements 14D, E). The scattered RFP$^+$ RUNX1$^-$ cells detected in
347 distal branches by day 7 often co-expressed NKX3.1 (Figures 7E, F). Overall, this indicates that
348 *Runx1* expressing cells only marginally contribute to the expansion of the NKX3.1 compartment
349 (Figure 7G). Finally, we wondered whether RUNX1$^+$ cells contributed to the establishment of
350 the proximal luminal lineage. We evaluated the proportion of RFP labelled cells co-expressing
351 K4, previously identified as a marker of the developing C2 and adult Lum-D populations (Figures
352 3D and 6H). Interestingly, the fraction of K4$^+$ RFP labeled cells increased from 56.9 ± 10.6% to
353 74.1 ± 3.0% between day 2 and 7 (Figures 7F, G). There was also an increase of RFP$^+$ cells
354 expressing *Nupr1*, another marker of the C2 cluster (Figure 7–figure supplements 14F-H). Taken

355 together, these results show that only a small subset of *Runx1* expressing cells contributes to

356 the expansion of NKX3.1^{+} lineage, found in the distal region of the developing prostatic buds.

357 Instead, the majority of *Runx1* expressing cells preferentially remain in the proximal region of

358 the premature buds, where the proximal luminal lineage is established.

359 **DISCUSSION**

360 In this study, we identified RUNX1 as a new marker of a luminal population enriched in
361 the proximal region of the prostatic ducts. By combining scRNA-seq profiling and genetic
362 lineage tracing of *Runx1* expressing cells, we show that RUNX1$^+$ PLCs present in the intact
363 prostate constitute a developmentally distinct and intrinsically castration-resistant luminal
364 lineage. We propose that proximal and distal lineages are separate luminal entities from the
365 earliest stages of prostate development. As such, our study provides novel insights into the
366 cellular composition and developmental hierarchy of the mouse prostate epithelium.

367

368 Until the recent advances in single-cell technologies, the prostate epithelial hierarchy
369 was mainly defined based on anatomical features of the basal and luminal layers, their
370 histological characteristics and the expression of a small subset of markers (Shen & Abate-Shen,
371 2010; Toivanen & Shen, 2017). Here we present two comprehensive scRNA-seq dataset
372 covering both the adult and the developing prostate. To our knowledge, this constitutes the
373 first comprehensive single-cell atlas covering both intact and castrated adult mouse prostates,
374 annotated by their lobe of origin. These datasets can be browsed interactively at
375 http://shiny.cruk.manchester.ac.uk/pscapp/. In particular, our adult scRNA-seq dataset
376 highlighted an extensive degree of cellular heterogeneity, in particular within the luminal
377 epithelia. Several studies recently made similar observations either focusing on the AP
378 (Karthaus et al., 2020), or the intact prostate (Crowley et al., 2020; Joseph et al., 2020).
379 Integration of these multiple datasets will provide a more global view of the transcriptional
380 landscape of the prostate epithelium.

381 Although mainly known as a master regulator of hematopoiesis, RUNX1 is increasingly
382 implicated in hormone-associated epithelia including malignant conditions such as prostate
383 cancer (Banach-Petrosky et al., 2007; Lie-A-Ling et al., 2020; Scheitz et al., 2012; Takayama et
384 al., 2015). Here, we identified a subset of RUNX1$^+$ luminal cells located in the proximal region of
385 the developing and adult prostate, referred to as RUNX1$^+$ PLCs, and corresponding to the Lum-D
386 cluster identified in our adult scRNA-seq dataset. Of note, this subset appears to be the
387 equivalent of the 'L2' (Karthaus et al., 2020) or 'LumP' (Crowley et al., 2020) clusters identified
388 in recent studies. We demonstrate that these RUNX1$^+$ PLCs exhibit a greater organoid forming
389 potential compared to the remaining luminal fraction, consistent with previous reports isolating
390 similar proximal populations using different markers such as SCA-1, TROP2 or CD26 (Crowley et
391 al., 2020; Goldstein et al., 2008; Karthaus et al., 2020; Kwon et al., 2016). Furthermore, RUNX1$^+$
392 PLCs predominantly formed unipotent K8$^+$ hollow organoids demonstrating their preferential
393 commitment to the luminal fate. The greater clonogenicity of RUNX1$^+$ PLCs may in fact be
394 linked to the gene expression profile of the corresponding Lum-D population, suggesting a
395 more immature epithelial state, committed to the luminal lineage but not the secretory
396 function of the prostate. It is therefore tempting to speculate that these cells act as a latent
397 niche of 'facultative' stem cells (Clevers & Watt, 2018), primed to generate a structured
398 prostatic epithelium under defined conditions.
399 Further characterization of RUNX1 expression in prostate development revealed a
400 consistent expression pattern with the adult. RUNX1$^+$ luminal cells were restricted to the most
401 proximal region of the developing prostate buds, both in embryos and UGS explant cultures.
402 Our scRNA-seq of the developing prostate revealed a broad basal identity, supporting the

403 presence of multipotent basal progenitors during embryonic development (Ousset et al., 2012;
404 Pignon et al., 2013), switching to unipotency postnatally (Tika et al., 2019). However, we
405 observed a distinct cluster (C2) that strongly resembled the adult Lum-D population, suggesting
406 an early branching event towards the proximal luminal fate at the onset of prostate
407 development. Subsequent lineage tracing experiments indicated that *Runx1* expressing cells
408 preferentially populate the emerging proximal luminal identity. It would be interesting to
409 determine if the adult Lum-A, Lum-B, and Lum-C derive from multipotent-basal progenitors or
410 from any specific clusters identified in the developing prostate. This appears to be the case at
411 least for the adult Lum-D/RUNX1^{+} PLCs which already emerges during embryonic specification.
412 Our data also sheds a light on the regenerative potential of specific epithelial
413 populations. Basal and luminal lineages have previously been shown to be largely self-sustained
414 using generic basal and luminal *Cre* drivers (Choi et al., 2012; Ousset et al., 2012). However,
415 whether distinct subpopulations of luminal cells contribute to the regeneration of the others
416 remains poorly understood (X. Wang et al., 2009; Yoo et al., 2016). Our characterization of
417 RUNX1^{+} PLCs and the detection of a wide variety of luminal populations in our adult prostate
418 scRNA-seq data highlights the possible existence of multiple self-contained luminal populations.
419 Indeed, *Runx1* driven genetic tracing experiments in regression-regeneration assays revealed
420 that RUNX1^{+} PLCs did not contribute to the regeneration of distal NKX3.1^{+} cells. It was however
421 evident that RUNX1^{+} PLCs are intrinsically castration resistant and capable of sustaining their
422 own lineage in the regenerated prostate. Recently, it was proposed that prostate epithelial
423 regeneration is driven by almost all luminal cells persisting in castrated prostates (Karthaus et
424 al., 2020). Our results are compatible with this model, but we further demonstrate that not all

425 luminal subsets retain the same *in vivo* regenerative potential in response to androgen
426 stimulation. Thus, we suggest that the model of self-sustained basal and luminal populations
427 might be extended to individual luminal subpopulations. This hypothesis should be tested in the
428 future using a more specific Lum-D *Cre* driver (e.g. *Krt4*/*Psca*). It will also be of interest to
429 investigate the self-sustenance of other luminal compartments using Lum-A, Lum-B and Lum-C
430 specific *Cre* drivers.
431
432 In light of the extensive contribution of RUNX transcription factors to developmental
433 processes (Mevel et al., 2019), our study suggests a possible functional role for *Runx1* in specific
434 lineages of the prostate epithelium, in particular in PLCs. Also, the broad expression of *Runx1*
435 after castration suggest that it may be a valuable marker of castration-resistant cells. Functional
436 links between RUNX factors and hormones, including AR have been previously reported
437 (Chimge et al., 2016; Lie-A-Ling et al., 2020; Little et al., 2014; Riggio & Blyth, 2017; Takayama et
438 al., 2015; van Bragt et al., 2014) and warrants further investigations. Along these lines, there
439 seem to be an intriguing parallel between the low or absent expression of *Runx1* in prostate
440 secretory cells with the documented downregulation of *Runx1* in secretory alveolar cells of the
441 mammary gland epithelium (van Bragt et al., 2014). Overall, our results suggest that *Runx1*, but
442 also *Runx2*, may be functionally involved in the development and maintenance of specific
443 subpopulations of the prostate epithelium. It would now be of particular interest to further
444 study the contribution of RUNX1 to prostate tumorigenesis. In light of the prognostic value of
445 RUNX1 in triple-negative breast cancer (Ferrari et al., 2014), it would also be important to
446 evaluate its biomarker potential in clinical cohorts of PCa samples.

447

448 In conclusion, we characterized the expression pattern of *Runx1* in the developing,
449 normal and castrated mouse prostate. We observed that *Runx1* marks proximal luminal cells,
450 which is a distinct luminal lineage emerging early during prostate specification, displaying
451 intrinsic castration-resistant and self-sustaining properties. Our results therefore reveal strong
452 intrinsic lineage differences within the luminal compartment. The emerging C2/Lum-D
453 population retains a more embryonic-like program which could relate to their intrinsic
454 castration-resistant potential and have broader relevance to cancer treatment. These results
455 warrant future investigation of this luminal subset in the context of cancer development, tumor
456 aggressiveness and treatment responses.

457 ## MATERIALS AND METHODS

458 **Animal work**

459 Animal experiments were approved by the Animal Welfare and Ethics Review Body
460 (AWERB) of the Cancer Research UK Manchester Institute and conducted according to the UK
461 Home Office Project Licence (PPL 70/8580). Genetic lineage-tracing experiments were
462 performed at the Beatson Biological Services Unit (PPL 70/8645 & P5EE22AEE) and approved by
463 the University of Glasgow AWERB. Mice were maintained in purpose-built facility in a 12-hour
464 light/dark cycle with continual access to food and water.

465

466 Immunocompetent wild-type ICR (CD-1) mice were purchased from Envigo. P1-*Runx1*:GFP
467 and P2-*Runx1*:RFP have been described previously (Draper et al., 2018; Sroczynska et al., 2009).
468 Colonies were maintained on a ICR (CD-1) background. C57Bl/6J *Runx1*$^{mER\text{-}CRE\text{-}mER}$ (Samokhvalov
469 et al., 2007) were provided by RIKEN (Japan). C57Bl/6J *Rosa26*$^{flox\text{-}stop\text{-}flox\text{-}tdRFP}$ mice (Luche et al.,
470 2007) were acquired from the European Mouse Mutant Archive (EMMA). For all transgenic
471 lines, routine genotyping was undertaken at weaning (3 weeks of age) by automated PCR
472 genotyping (Transnetyx). For timed mating experiments, vaginal plug detection was considered
473 as embryonic day (E) 0.5.

474

475 All animal procedures were performed on adult males at least 7 weeks of age. Surgical
476 castration was carried out under aseptic conditions. For prostate regeneration assays,
477 testosterone pellets (Belma Technologies) were implanted subcutaneously. For *in vivo* genetic
478 lineage-tracing experiments, tamoxifen (Sigma, T5648) was resuspended in ethanol and diluted

479 in corn oil at a concentration of 10 mg/mL and administered via intra-peritoneal injections daily
480 for 4 consecutive days using the following regimen: 3mg, 2mg, 2mg, 2mg.
481
482 **Isolation of mouse prostate cells**
483 All dissections were performed under a stereo microscope in sterile PBS. Dissociated murine
484 prostate cells were obtained by digesting pre-minced prostate tissue for 1h at 37˚C in digestive
485 medium prepared in prepared in ADMEM/F12 (Gibco), and containing 1mg/mL Collagenase
486 Type I (ThermoFischer Scientific, #17018029), 1mg/mL Dispase II (ThermoFischer Scientific,
487 #17105041), 10% Fetal Bovine Serum (Gibco), 1% Penicillin-Streptomycin-Glutamine (Sigma),
488 and 10 µM Y-27632 dyhydrochloride (Chemdea, #CD0141). For embryonic urogenital sinuses
489 (UGS), dissociation time was reduced to 30 min. Single cells were obtained after an additional
490 10 min incubation in TrypLE (Gibco) at 37˚C before mechanical dissociation with a syringe and
491 needle (25G). Cells were then filtered through a 50 µm cell strainer.
492
493 **Flow-cytometry and cell-sorting**
494 Single cell suspensions were kept in Advanced DMEM/F-12 (Gibco) containing 5% FBS
495 supplemented with 10 µM Y-27632. Cells were incubated for 10 min using unconjugated anti-
496 mouse CD16/32 antibody (Biolegend, C93, #101301) at 4˚C prior to labelling with specific
497 fluorochrome-labelled antibodies. Details of FACS reagents and antibodies are listed in Table 3.
498 Cells were filtered through a 50 µm cell strainer prior to acquisition. Hoechst 33258 or Sytox
499 blue (ThermoFischer Scientific) were used as viability stains. Single-cell suspensions were

500 analyzed on a Fortessa (BD Biosciences) and sorts were performed on a FACSAriaIII (BD
501 Biosciences). FACS data were analyzed using FlowJo software (BD Life Sciences).
502
503 **Organoid formation assays**
504 *In vitro* organoid formation assays were performed as described in Drost et al., 2016. Single
505 cells were resuspended in 40 µL drops of phenol red-free Cultrex RGF BME Type 2 (BME 2,
506 Amsbio, #3533-005-02), and seeded in CellCarrier-96 Ultra Microplates (PerkinElmer,
507 #6055302). Defined organoid culture medium was prepared with Advanced DMEM/F-12
508 (Gibco), supplemented with 10 mM Hepes (Sigma), Gutamax (Gibco), Penicillin/Streptomycin
509 (Sigma), B27 (Life Technologies, 17504-044), 50 mg/mL EGF (PeproTech, #AF-100-15), 500
510 ng/mL R-spondin 1 (R&D Systems, #4645-RS), 100 ng/mL Noggin (R&D Systems, #6057-NG), 10
511 mM Y-27632 dyhydrochloride (Chemdea, #CD0141), 200nM A83-01 (Tocris Bioscience, #2939),
512 1.25 mM N-Acetylcystein (Sigma), and 1 nM Dihydrotestosterone (DHT, Sigma #730637).
513 Medium was refreshed every 2-3 days, and organoid cultures were scored after 7 days.
514
515 **UGS explant cultures**
516 UGS explant cultures were performed as described previously (Kruithof-de Julio et al.,
517 2013). Briefly, E15.5 embryos were obtained from timed matings. Urogenital sinuses (UGS)
518 were isolated from the embryos and cultured using a Durapore Membrane Filter 0.65 µm
519 (#DVPP02500) placed on a stainless-steel mesh for up to 7 days in Ham's F-12/DMEM (Gibco)
520 supplemented with Insulin-Transferrin-Sodium Selenite Supplement (Roche) and 10 µM
521 dihydrotestosterone (Sigma). Media were renewed every 2-3 days. For lineage-tracing

522 experiments, tamoxifen-induced labelling was performed using 0.5 µM 4-hydroxytamoxifen
523 (#T176, Sigma).
524
525 **Immunohistochemistry**
526 Prostate tissues were harvested and fixed in 10% buffered formalin for 24h. Fixed tissues
527 were processed using standard procedures and embedded in paraffin. Formalin-fixed paraffin-
528 embedded (FFPE) sections (4 µm) were cut and dried overnight at 37°C. Multiplexed
529 immunofluorescent stainings of FFPE sections were performed on an automated Leica BOND RX
530 platform using the Opal multiplexing workflow (PerkinElmer). In brief, sections were dewaxed,
531 and rehydrated, and endogenous peroxidase activity was quenched by 10 min pre-treatment
532 with 3% hydrogen peroxide diluted in TBS-T (Tris-Buffered Saline 0.05% Tween-20). Following
533 on-board heat-induced epitope retrieval with citrate buffer (pH 6.0) for 20 min, sections were
534 incubated for 10 min with 10% Casein (Vector Laboratories) diluted in TBS-T. Each staining cycle
535 included a primary antibody incubation for 30 min, followed by buffer washes, and 30 min
536 incubation with HRP labelled secondary antibodies (Table 2). After further washes, the
537 Tyramide labeled with a fluorophore (Opal 520, Opal 570 or Opal 650, PerkinElmer) was added
538 for a final 10 min. Subsequent antibody stainings were performed by repeating the same
539 procedure, separated by heat-mediated antibody denaturation using citrate buffer (pH 6.0) for
540 5 min at 95°C. Nuclei were counterstained with DAPI (Sigma) and slides were sealed using
541 ProLong Gold Antifade Mountant (ThermoFischer Scientific). *In situ* hybridization (ISH) to detect
542 *Nupr1* (ACD, LS 2.5 Mm-Nupr1 #434818) was done using the Multiplex Fluorescent detection kit
543 (ACD) on the automated Leica BOND RX platform following the manufacturer's instructions.

544 Pre-treatment was done using an EDTA based pH 9.0 epitope retrieval solution for 15 min at
545 88°C followed by 10 min protease incubation. After ISH, antibody staining was carried out using
546 an anti-RFP antibody for 1h detected with EnVision HRP anti-rabbit secondary (Agilent)
547 followed by incubation with Tyramide-conjugated Opal 570 (PerkinElmer) as described above.
548 Anti-CDH1 antibody was applied for 1h and detected using an anti-goat Alexa Fluor 647
549 secondary antibody (ThermoFischer Scientific, #A-21447). Staining of frozen sections was
550 performed as described previously (Thambyrajah et al., 2016). The list of antibodies used is
551 available in Table 1.
552
553 **Image acquisition and analysis**
554 Whole-slide images were acquired on an Olympus VS120 slide scanner. Images were
555 analyzed using QuPath v0.2 (Bankhead et al., 2017). Briefly, annotations were drawn manually
556 to select areas of interest. Nuclear detection was achieved using the "cell detection" module on
557 the DAPI channel. A classifier was then trained for each batch of images using the random
558 forest algorithm, to detect the epithelial layers based on either CDH1 or K5/K8 stainings. Single-
559 cell intensity measurements were analyzed using R (3.6.3). For Quantitative Imaged-Based
560 Cytometry (QBIC), single-cell intensity measurements were log10 transformed and plotted
561 using the 'geom_hex' function of the ggplot2 R package. QuPath was used to extract
562 representative high-quality raw images of selected areas from whole slide images using the
563 'Send region to ImageJ' tool. Images used for publication were processed with ImageJ (NIH
564 Image, Maryland, USA). Confocal images were acquired using a Leica TCS SP8 confocal

565 microscope and LAS X Leica software. Images of whole UGS explant culture were taken using a
566 Leica MZ FLIII microscope.
567
568 **Whole-mount immunofluorescent staining of organoids**
569 Whole-mount staining was adapted from Yokomizo et al., 2012. Organoids were fixed
570 directly in 96-well plates using 4% paraformaldehyde for 1h at 4°C. After 3 washes of 5 min in
571 PBS, organoids were incubated in PBS-BST, containing PBS, 1% milk, 1% BSA, 10% goat serum
572 (Agilent, #X090710), 0.4% Triton X-100. Pre-conjugated primary antibodies, K5 Alexa Fluor 647
573 (#ab193895, Abcam) and K8 Alexa Fluor 488 (#ab192467, Abcam) were diluted at 1/400 in PBS-
574 BST and incubated with the organoids overnight at 4°C on a rocking platform. After 3 washes of
575 1h in PBS-BST at 4°C, organoids were stained with DAPI at 2 µg/mL diluted in PBS-BST and
576 incubated for another 30 min at 4°C on a rocking platform. Images were acquired on an Opera
577 Phenix High Content Screening System using the 10x air and 20x water lenses. Quantitative
578 analysis was performed using the Harmony software on maximum projection images.
579
580 **scRNA-seq sample preparation**
581 A detailed description of the samples, replicates, and the corresponding cellular populations
582 used for each sequencing run is provided in Supplementary file 1. For the adult mouse prostate
583 dataset, AP, DLP, and VP lobes were micro dissected and pooled from P2-*Runx1*:RFP reporter
584 mice after dissociation. Single live EPCAM^{+} cells from RFP^{+} and RFP^{-} fractions of each lobes were
585 sorted separately (containing a mix of CD49f^{high} basal and CD24^{high} luminal cells). For the UGS
586 explant culture dataset, the middle regions of the explants were micro dissected to enrich for

587 prostatic branching events and pooled by time point after dissociation. Single live EPCAM+ cells
588 were sorted for each independent time point.
589
590 **scRNA-seq sample multiplexing**
591 Individually sorted populations were multiplexed using the MULTI-seq protocol (McGinnis
592 et al., 2019). Reagents were kindly provided by Dr. Zev Gartner. In brief, after sorting, cells were
593 washed once in cold serum- and BSA-free PBS. A lipid-modified DNA oligonucleotide and a
594 specific sample barcode oligonucleotide were then mixed and added to the cells at a final
595 concentration of 200 nM each, and incubated in cold PBS for 5 min. Each individual sample to
596 be multiplexed received an independent sample barcode. Next, a common lipid-modified co-
597 anchor was added at 200 nM to each sample to stabilize the membrane bound barcodes. After
598 an additional 5 min incubation on ice, cells were washed 2 times with PBS containing 1% FBS 1%
599 BSA in order to quench unbound barcodes. Samples were then pooled together and washed
600 once with PBS 1% FBS 1% BSA. After cell counting, cells were loaded in a Chromium Single Cell
601 3' GEM Library & Gel Bead Kit v3 (10x Genomics).
602
603 **scRNA-seq library preparation, sequencing and pre-processing**
604 Gene expression (cDNA) libraries were prepared according to the manufacturer's protocol.
605 MULTI-seq barcode libraries were separated from the cDNA libraries during the first round of
606 size selection, and PCR amplified prior to sequencing according to the MULTI-seq library
607 preparation protocol (McGinnis et al., 2019). For the adult mouse prostate dataset, cDNA
608 libraries of 'run 1' and 'run 2' were sequenced on Illumina NovaSeq 6000 System, and 'run 3'

609 was sequenced on Illumina HiSeq 2500. The UGS mouse prostate explant run was also
610 sequenced on Illumina HiSeq 2500. Sequencing data of cDNA libraries were processed using
611 Cellranger v3.1.0 and mapped onto mm10 mouse reference genome. Pre-processing of the
612 MULTI-seq library fastq files was performed using the 'deMULTIplex' (v1.0.2) R package
613 (https://github.com/chris-mcginnis-ucsf/MULTI-seq) to generate a sample barcode UMI count
614 matrix. Detailed quality control metrics of each sequencing run are provided in Supplementary
615 file 1.
616
617 **Adult mouse prostate dataset analysis**
618 *Quality control and barcode demultiplexing of individual runs.* Each run was pre-processed
619 individually prior data integration. Cellranger outputs were loaded into the R package Seurat
620 (v3.1.5). Cells were kept if they had more than 750 detected genes, less than 7500 UMIs and
621 less than 10% mitochondrial transcripts. Sample barcodes were demultiplexed using the
622 HTODemux function implemented in Seurat. Briefly, a negative binomial distribution was used
623 to estimate the background levels based on *k*-means clustering of the barcode normalized
624 counts. Barcodes with values above the 99% quantile were considered 'positive' for a given
625 sample. Cells positive for more than one barcode were considered as 'doublets'. Doublets and
626 negative cells were excluded for all downstream analyses. Thresholds were empirically adjusted
627 to remove additional cells with possible ambiguous classification (Supplementary file 1). Of
628 note, in both 'run 1' and 'run 2', a large number of cells were classified 'negative' due to the
629 failed labelling of 'Bar3' (corresponding to 'Intact DLP RFP+' sample). For these runs, we used
630 DoubletFinder (McGinnis et al., 2019) to remove predicted doublets missed out as a

631 consequence of the failed labeling of 'Bar3'. After classification, barcodes were represented in
632 UMAP space to confirm the purity of the barcode assignment obtained for each sample (Figure
633 3–figure supplement 5A). We obtained a total of 4,499 cells from 3 independent experiments.
634
635 *Integration, low dimensional embedding and clustering.* Data aggregation was performed
636 according to the standard integration procedure implemented in Seurat. In brief, each dataset
637 was log normalized, and 3000 variable features were initially computed using the 'vst' method.
638 For integration, 2000 features and 50 dimensions were used as anchors. Integrated data were
639 scaled and the first 50 principal components (PC) were calculated for downstream analyses.
640 Uniform Manifold Approximation and Projection (UMAP) (McInnes et al., 2018) was used for
641 visualization. Graph-based louvain clustering was performed on a shared nearest neighbor
642 graph constructed using 20 nearest neighbors for every cell, and a resolution of 0.4, which gave
643 a reasonable segmentation of the data (Figure 3–figure supplement 5B,C). Extensive
644 exploration of each cluster based on known marker genes was then carried out to subset
645 prostate epithelial cells. We found 10 prostate epithelial clusters (*Epcam*, *Krt8*, *Cd24a*, *Spink1*,
646 *Krt19*, *Tacstd2*, *Psca*, *Krt4*, *Tgm4*, *Nkx3-1*, *Pbsn*, *Msmb*, *Piezo2*, *Trp63*, *Krt5*, *Krt14*), 3 clusters of
647 hematopoietic cells (*Vim*, *Ptprc*, *Cd74*, *Itgam*, *Cd3d*), 1 cluster of endothelial cells (*Pecam1*), 1
648 cluster of fibroblasts (*Vim*, *Col1a1*) and 1 cluster of mesonephric derivatives (*Svs2*, *Pax2*) (Figure
649 3–figure supplement 5D,E).
650
651 *Analysis of prostate epithelial populations.* The same dimension reduction approach described
652 above was performed on the selected prostate epithelial clusters, using a resolution of 0.3 for

653 graph-based louvain clustering. We annotated 1 large population of basal cells by merging 3
654 subclusters highly expressing *Krt5*, *Krt14* and *Trp63* as we did not discuss the heterogeneity of
655 the basal compartment in this study (Figures 3B-D; Figure 3–figure supplement 6F,I). We
656 annotated the different luminal clusters expressing higher levels of *Cd26*/*Dpp4, Cd24a*, *Krt8* and
657 *Krt18*, as Lum-A, Lum-B, Lum-C, Lum-D, Lum-E and Lum-F. Several genes specifically marked
658 each cluster, including *Sbp*/*Spink1* in Lum-A, *Tgm4* in Lum-B, *Msmb* in Lum-C, *Psca*/*Krt4* in Lum-
659 D, *Basp1*/*Lpl* in Lum-E, and *Crym* in Lum-F (Figures 3C, D; Figure 3–figure supplement 7A). Data
660 were then imported in Scanpy (v1.4.6) to infer lineage relationships between cellular
661 populations via partition-based graph abstraction (PAGA) implemented in the tl.paga function
662 (Wolf et al., 2019). Briefly, a single cell neighborhood graph (n_neighbors = 50) was computed
663 using the integrated principal components previously calculated in Seurat. PAGA was generated
664 based on our annotated clusters. The final UMAP representation was generated using PAGA-
665 initialised positions to better preserve the global topology of the data. All final data
666 visualizations were generated in R.
667
668 *Differential gene expression analysis and gene ontology.* Differential gene expression analyses
669 between clusters were performed using the MAST method (Finak et al., 2015) implemented in
670 Seurat within the 'FindAllMarkers' and 'FindMarkers' functions. Testing was limited to genes
671 detected in at least 25% of the tested populations (min.pct = 0.25) and showing at least ± 0.25
672 log fold change difference (logfc.threshold = 0.25). The 'g:GOSt' function of the gprofiler2 R
673 package was used to perform functional enrichment analysis on gene ontology terms (GO:BP,

674 biological processes). Genes showing at least 0.50 log fold change enrichment in the group
675 tested were kept.
676
677 **UGS explant cultures dataset**
678 A similar strategy was applied for the analysis of the UGS explant culture dataset, with some
679 alterations described below.
680
681 *Quality control and barcode demultiplexing.* Cells were kept if they had more than 1000
682 detected genes, and less than 7.5% mitochondrial transcripts. Barcode classification was
683 performed as above, using the 90% quantile in 'HTODemux' (Figure 6–figure supplement 12A).
684 We obtained a total of 5,122 cells that passed quality control from the 4 time points.
685
686 *Low dimensional embedding and clustering.* The first 50 principal components and 20 neighbors
687 were used for UMAP visualization. Graph-based clustering was done using a resolution
688 parameter of 0.3. We noticed a strong effect of cell cycle using cell cycles genes defined in
689 Tirosh et al., 2016. This was particularly evident using the 'CellCycleScoring' function
690 implemented in Seurat (Figure 6–figure supplement 12B). To minimize the impact of cell cycle
691 on downstream analyses, the cell cycle scores were regressed out during data scaling. We
692 identified 6 main clusters, that we annotated based on the expression of several marker genes
693 (Figure 6–figure supplement 12C-E). We identified 2 clusters of developing mesonephric
694 derivatives (*Hoxb7*, *Wfdc2*, *Gata3*, *Sox17*, *Pax2*, *Pax8*, *Lhx1*), 1 cluster of developing bladder
695 urothelium (*Upk3a*, *Foxq1*, *Plaur*, *Krt7*, *Krt20*), 1 cluster of mesenchymal cells (*Vim*, *Col3a1*,

696 *Col1a1*, *Pdgfra*, *Zeb1*) and 1 cluster corresponding to the developing prostatic epithelium
697 (*Epcam*, *Krt8*, *Krt5*, *Krt14*, *Krt15*, *Shh*, *Hoxb13*, *Hoxd13*, *Nkx3-1*). We also identified one cluster
698 largely associated with hypoxia and cellular stress ontologies (Figure 6–figure supplement 12F).
699
700 *Analysis of the developing prostatic epithelium.* The same dimension reduction approach was
701 initially applied on the developing prostatic cluster. After graph-based clustering using a
702 resolution of 0.5, 10 clusters were identified and visualized via UMAP (Figure 6–figure
703 supplement 12G-J). We computed diffusion components using 'runDiffusionMap'
704 (ncomponents = 20, k = 20) implemented in the scater (v1.14.6) R package. We found the small
705 cluster C9 to be largely diverging from the remainder fraction in diffusion space, therefore it
706 was excluded for downstream analysis (Figure 6–figure supplement 12K). We then imported
707 the data in Scanpy and used the first 10 diffusion components to compute a neighborhood
708 graph (n_neighbors = 20) which was used for PAGA. We finally computed a force-direct layout
709 (ForceAtlas2) using PAGA-initialised positions.
710
711 *Analysis of gene set activity.* Gene signatures were generated from the list of differentially
712 expressed genes by keeping those showing at least 0.50 log fold change enrichment in each
713 given group. Gene lists were used as custom gene sets (Supplementary file 5) in the AUCell
714 (Aibar et al., 2017) R package (v1.8.0). Briefly, AUCell uses the Area Under the Curve to evaluate
715 the enrichment of a given gene set in each cell, in a ranking based manner. It outputs an AUC
716 score for each individual cell, which is used to explore the relative expression of the signature.

717 Per cell AUC scores of each signatures were overlayed on the dimension reduction layout and
718 plotted as boxplots to visualize enrichments across the different cellular subsets.
719
720 **Data availability**
721 Raw sequencing files and processed gene expression matrices have been deposited in the
722 NCBI Gene Expression Omnibus under the accession number GSE151944. The processed
723 datasets for both mouse adult prostate and UGS prostate explant cultures can be accessed via a
724 searchable R Shiny application available at http://shiny.cruk.manchester.ac.uk/pscapp/. All
725 code used to process data and generate figures will be made available on a public GitHub
726 repository upon publication.
727
728 **Statistical analyses**
729 Statistical analyses were performed using Graphpad/Prism (v8.4.2). Data are
730 represented as mean ±SD. Two-tailed unpaired *t*-tests were used to compare means between
731 two groups. Statistical significance was set at $p < 0.05$. For animal model studies, no statistical
732 method was used to pre-determine the sample size. No randomization or blinding was used for
733 *in vivo* studies.
734
735

ACKNOWLEDGEMENTS

We thank the laboratories' members for critical reading of the manuscript, in particular Dr. Michael Lie-a-ling, Dr. Alice Lallo and Catherine Winchester. We thank the staff at the Histology, Flow Cytometry, Advanced Imaging, Molecular Biology, and Breeding Unit Core facilities of CRUK Manchester Institute, as well as the CRUK Beatson Biological Services Unit and Flow Cytometry Core facility for technical support. We thank Dr. Zev Gartner for kindly providing the MULTI-seq reagents. We thank Dr. Kirsteen Campbell with assistance on the lineage tracing experiments. We thank Dr. Berenika Plusa and Dr. Roberto de la Fuente with assistance on timed matings experiments. We thank Professor Hans Jorg Fehling and the European Mouse Mutant Archive for providing the Rosa26$^{flox\text{-}stop\text{-}flox\text{-}tdRFP}$ mice. This research was supported by CRUK core funding C5759/A20971 (G.L. and E.B., CRUK Manchester Institute) and C596/A17196 (K.B., CRUK Beatson Institute).

AUTHORS CONTRIBUTION

Conceptualization, R.M., E.B., K.B., and G.L.; Methodology, R.M., E.B., K.B., and G.L.; Formal analysis, R.M.; Data curation, R.M.; Investigation, R.M., I.S., S.M., L.G., R.P., M.Z.F.; Writing – Original Draft, R.M.; Writing – Review & Editing, R.M., I.S., K.B., E.B., G.L.; Resources, P.O., H.Y.L and I.A.; Supervision, E.B., K.B. and G.L.; Project Administration, G.L.; Funding Acquisition, E.B., K.B. and G.L.

COMPETING INTERESTS

The authors declare no competing interests.

758 **REFERENCES**

759 Aibar, S., González-Blas, C. B., Moerman, T., Huynh-Thu, V. A., Imrichova, H., Hulselmans, G.,
760 Rambow, F., Marine, J.-C., Geurts, P., Aerts, J., van den Oord, J., Atak, Z. K., Wouters, J.,
761 & Aerts, S. (2017). SCENIC: Single-cell regulatory network inference and clustering.
762 *Nature Methods*, *14*(11), 1083–1086. https://doi.org/10.1038/nmeth.4463

763 Banach-Petrosky, W., Jessen, W. J., Ouyang, X., Gao, H., Rao, J., Quinn, J., Aronow, B. J., &
764 Abate-Shen, C. (2007). Prolonged exposure to reduced levels of androgen accelerates
765 prostate cancer progression in Nkx3.1; Pten mutant mice. *Cancer Research*, *67*(19),
766 9089–9096. https://doi.org/10.1158/0008-5472.CAN-07-2887

767 Bankhead, P., Loughrey, M. B., Fernández, J. A., Dombrowski, Y., McArt, D. G., Dunne, P. D.,
768 McQuaid, S., Gray, R. T., Murray, L. J., Coleman, H. G., James, J. A., Salto-Tellez, M., &
769 Hamilton, P. W. (2017). QuPath: Open source software for digital pathology image
770 analysis. *Scientific Reports*, *7*(1), 16878. https://doi.org/10.1038/s41598-017-17204-5

771 Barros-Silva, J. D., Linn, D. E., Steiner, I., Guo, G., Ali, A., Pakula, H., Ashton, G., Peset, I., Brown,
772 M., Clarke, N. W., Bronson, R. T., Yuan, G.-C., Orkin, S. H., Li, Z., & Baena, E. (2018).
773 Single-Cell Analysis Identifies LY6D as a Marker Linking Castration-Resistant Prostate
774 Luminal Cells to Prostate Progenitors and Cancer. *Cell Reports*, *25*(12), 3504-3518.e6.
775 https://doi.org/10.1016/j.celrep.2018.11.069

776 Berman, D. M., Desai, N., Wang, X., Karhadkar, S. S., Reynon, M., Abate-Shen, C., Beachy, P. A.,
777 & Shen, M. M. (2004). Roles for Hedgehog signaling in androgen production and
778 prostate ductal morphogenesis. *Developmental Biology*, *267*(2), 387–398.
779 https://doi.org/10.1016/j.ydbio.2003.11.018

780 Bhatia-Gaur, R., Donjacour, A. A., Sciavolino, P. J., Kim, M., Desai, N., Young, P., Norton, C. R.,
781 Gridley, T., Cardiff, R. D., Cunha, G. R., Abate-Shen, C., & Shen, M. M. (1999). Roles for
782 Nkx3.1 in prostate development and cancer. *Genes & Development*, *13*(8), 966–977.
783 Browne, G., Taipaleenmäki, H., Bishop, N. M., Madasu, S. C., Shaw, L. M., van Wijnen, A. J.,
784 Stein, J. L., Stein, G. S., & Lian, J. B. (2015). Runx1 is associated with breast cancer
785 progression in MMTV-PyMT transgenic mice and its depletion in vitro inhibits migration
786 and invasion. *Journal of Cellular Physiology*, *230*(10), 2522–2532.
787 https://doi.org/10.1002/jcp.24989
788 Burger, P. E., Xiong, X., Coetzee, S., Salm, S. N., Moscatelli, D., Goto, K., & Wilson, E. L. (2005).
789 Sca-1 expression identifies stem cells in the proximal region of prostatic ducts with high
790 capacity to reconstitute prostatic tissue. *Proceedings of the National Academy of*
791 *Sciences of the United States of America*, *102*(20), 7180–7185.
792 https://doi.org/10.1073/pnas.0502761102
793 Chimge, N.-O., Little, G. H., Baniwal, S. K., Adisetiyo, H., Xie, Y., Zhang, T., O'Laughlin, A., Liu, Z.
794 Y., Ulrich, P., Martin, A., Mhawech-Fauceglia, P., Ellis, M. J., Tripathy, D., Groshen, S.,
795 Liang, C., Li, Z., Schones, D. E., & Frenkel, B. (2016). RUNX1 prevents oestrogen-
796 mediated AXIN1 suppression and β-catenin activation in ER-positive breast cancer.
797 *Nature Communications*, *7*, 10751. https://doi.org/10.1038/ncomms10751
798 Choi, N., Zhang, B., Zhang, L., Ittmann, M., & Xin, L. (2012). Adult murine prostate basal and
799 luminal cells are self-sustained lineages that can both serve as targets for prostate
800 cancer initiation. *Cancer Cell*, *21*(2), 253–265. https://doi.org/10.1016/j.ccr.2012.01.005

801 Chua, C. W., Shibata, M., Lei, M., Toivanen, R., Barlow, L. J., Bergren, S. K., Badani, K. K.,
802 McKiernan, J. M., Benson, M. C., Hibshoosh, H., & Shen, M. M. (2014). Single luminal
803 epithelial progenitors can generate prostate organoids in culture. *Nature Cell Biology*,
804 *16*(10), 951–961, 1–4. https://doi.org/10.1038/ncb3047
805 Clevers, H., & Watt, F. M. (2018). Defining Adult Stem Cells by Function, not by Phenotype.
806 *Annual Review of Biochemistry*, *87*(1), 1015–1027. https://doi.org/10.1146/annurev-
807 biochem-062917-012341
808 Crowell, P. D., Fox, J. J., Hashimoto, T., Diaz, J. A., Navarro, H. I., Henry, G. H., Feldmar, B. A.,
809 Lowe, M. G., Garcia, A. J., Wu, Y. E., Sajed, D. P., Strand, D. W., & Goldstein, A. S. (2019).
810 Expansion of Luminal Progenitor Cells in the Aging Mouse and Human Prostate. *Cell*
811 *Reports*, *28*(6), 1499-1510.e6. https://doi.org/10.1016/j.celrep.2019.07.007
812 Crowley, L., Cambuli, F., Aparicio, L., Shibata, M., Robinson, B. D., Xuan, S., Li, W., Hibshoosh, H.,
813 Loda, M., Rabadan, R., & Shen, M. M. (2020). A single-cell atlas of the mouse and human
814 prostate reveals heterogeneity and conservation of epithelial progenitors. *BioRxiv*,
815 2020.05.29.123836. https://doi.org/10.1101/2020.05.29.123836
816 Doles, J. D., Vezina, C. M., Lipinski, R. J., Peterson, R. E., & Bushman, W. (2005). Growth,
817 morphogenesis, and differentiation during mouse prostate development in situ, in renal
818 grafts, and in vitro. *The Prostate*, *65*(4), 390–399. https://doi.org/10.1002/pros.20321
819 Draper, J. E., Sroczynska, P., Fadlullah, M. Z. H., Patel, R., Newton, G., Breitwieser, W., Kouskoff,
820 V., & Lacaud, G. (2018). A novel prospective isolation of murine fetal liver progenitors to
821 study in utero hematopoietic defects. *PLoS Genetics*, *14*(1), e1007127.
822 https://doi.org/10.1371/journal.pgen.1007127

823 Drost, J., Karthaus, W. R., Gao, D., Driehuis, E., Sawyers, C. L., Chen, Y., & Clevers, H. (2016).
824 Organoid culture systems for prostate epithelial and cancer tissue. *Nature Protocols*,
825 *11*(2), 347–358. https://doi.org/10.1038/nprot.2016.006
826 English, H. F., Santen, R. J., & Isaacs, J. T. (1987). Response of glandular versus basal rat ventral
827 prostatic epithelial cells to androgen withdrawal and replacement. *The Prostate*, *11*(3),
828 229–242.
829 Ferrari, N., Mohammed, Z. M. A., Nixon, C., Mason, S. M., Mallon, E., McMillan, D. C., Morris, J.
830 S., Cameron, E. R., Edwards, J., & Blyth, K. (2014). Expression of RUNX1 Correlates with
831 Poor Patient Prognosis in Triple Negative Breast Cancer. *PLoS ONE*, *9*(6), e100759.
832 https://doi.org/10.1371/journal.pone.0100759
833 Finak, G., McDavid, A., Yajima, M., Deng, J., Gersuk, V., Shalek, A. K., Slichter, C. K., Miller, H. W.,
834 McElrath, M. J., Prlic, M., Linsley, P. S., & Gottardo, R. (2015). MAST: A flexible statistical
835 framework for assessing transcriptional changes and characterizing heterogeneity in
836 single-cell RNA sequencing data. *Genome Biology*, *16*(1), 278.
837 https://doi.org/10.1186/s13059-015-0844-5
838 Georgas, K. M., Armstrong, J., Keast, J. R., Larkins, C. E., McHugh, K. M., Southard-Smith, E. M.,
839 Cohn, M. J., Batourina, E., Dan, H., Schneider, K., Buehler, D. P., Wiese, C. B., Brennan, J.,
840 Davies, J. A., Harding, S. D., Baldock, R. A., Little, M. H., Vezina, C. M., & Mendelsohn, C.
841 (2015). An illustrated anatomical ontology of the developing mouse lower urogenital
842 tract. *Development (Cambridge, England)*, *142*(10), 1893–1908.
843 https://doi.org/10.1242/dev.117903

844 Goldstein, A. S., Lawson, D. A., Cheng, D., Sun, W., Garraway, I. P., & Witte, O. N. (2008). Trop2
845 identifies a subpopulation of murine and human prostate basal cells with stem cell
846 characteristics. *Proceedings of the National Academy of Sciences of the United States of*
847 *America*, *105*(52), 20882–20887. https://doi.org/10.1073/pnas.0811411106
848 Goto, K., Salm, S. N., Coetzee, S., Xiong, X., Burger, P. E., Shapiro, E., Lepor, H., Moscatelli, D., &
849 Wilson, E. L. (2006). Proximal Prostatic Stem Cells Are Programmed to Regenerate a
850 Proximal-Distal Ductal Axis. *STEM CELLS*, *24*(8), 1859–1868.
851 https://doi.org/10.1634/stemcells.2005-0585
852 Höfner, T., Eisen, C., Klein, C., Rigo-Watermeier, T., Goeppinger, S. M., Jauch, A., Schoell, B.,
853 Vogel, V., Noll, E., Weichert, W., Baccelli, I., Schillert, A., Wagner, S., Pahernik, S., Sprick,
854 M. R., & Trumpp, A. (2015). Defined Conditions for the Isolation and Expansion of Basal
855 Prostate Progenitor Cells of Mouse and Human Origin. *Stem Cell Reports*, *4*(3), 503–518.
856 https://doi.org/10.1016/j.stemcr.2015.01.015
857 Horton, C., Liu, Y., Yu, C., Xie, Q., & Wang, Z. A. (2019). Luminal-contact-inhibition of epithelial
858 basal stem cell multipotency in prostate organogenesis and homeostasis. *Biology Open*,
859 *8*(10). https://doi.org/10.1242/bio.045724
860 Joseph, D. B., Henry, G. H., Malewska, A., Iqbal, N. S., Ruetten, H. M., Turco, A. E., Abler, L. L.,
861 Sandhu, S. K., Cadena, M. T., Malladi, V. S., Reese, J. C., Mauck, R. J., Gahan, J. C.,
862 Hutchinson, R. C., Roehrborn, C. G., Baker, L. A., Vezina, C. M., & Strand, D. W. (2020).
863 Urethral luminal epithelia are castration-insensitive cells of the proximal prostate. *The*
864 *Prostate*. https://doi.org/10.1002/pros.24020

865 Karthaus, W. R., Hofree, M., Choi, D., Linton, E. L., Turkekul, M., Bejnood, A., Carver, B.,
866 Gopalan, A., Abida, W., Laudone, V., Biton, M., Chaudhary, O., Xu, T., Masilionis, I.,
867 Manova, K., Mazutis, L., Pe'er, D., Regev, A., & Sawyers, C. L. (2020). Regenerative
868 potential of prostate luminal cells revealed by single-cell analysis. *Science*, *368*(6490),
869 497–505. https://doi.org/10.1126/science.aay0267
870 Karthaus, W. R., Iaquinta, P. J., Drost, J., Gracanin, A., van Boxtel, R., Wongvipat, J., Dowling, C.
871 M., Gao, D., Begthel, H., Sachs, N., Vries, R. G. J., Cuppen, E., Chen, Y., Sawyers, C. L., &
872 Clevers, H. C. (2014). Identification of multipotent luminal progenitor cells in human
873 prostate organoid cultures. *Cell*, *159*(1), 163–175.
874 https://doi.org/10.1016/j.cell.2014.08.017
875 Keil, K. P., Mehta, V., Abler, L. L., Joshi, P. S., Schmitz, C. T., & Vezina, C. M. (2012). Visualization
876 and quantification of mouse prostate development by in situ hybridization.
877 *Differentiation; Research in Biological Diversity*, *84*(3), 232–239.
878 https://doi.org/10.1016/j.diff.2012.07.005
879 Keita, M., Bachvarova, M., Morin, C., Plante, M., Gregoire, J., Renaud, M.-C., Sebastianelli, A.,
880 Trinh, X. B., & Bachvarov, D. (2013). The RUNX1 transcription factor is expressed in
881 serous epithelial ovarian carcinoma and contributes to cell proliferation, migration and
882 invasion. *Cell Cycle (Georgetown, Tex.)*, *12*(6), 972–986.
883 https://doi.org/10.4161/cc.23963
884 Kruithof-de Julio, M., Shibata, M., Desai, N., Reynon, M., Halili, M. V., Hu, Y.-P., Price, S. M.,
885 Abate-Shen, C., & Shen, M. M. (2013). Canonical Wnt signaling regulates Nkx3.1
886 expression and luminal epithelial differentiation during prostate organogenesis.

887 *Developmental Dynamics : An Official Publication of the American Association of*
888 *Anatomists*, *242*(10), 1160–1171. https://doi.org/10.1002/dvdy.24008
889 Kwon, O.-J., Zhang, L., Ittmann, M. M., & Xin, L. (2014). Prostatic inflammation enhances basal-
890 to-luminal differentiation and accelerates initiation of prostate cancer with a basal cell
891 origin. *Proceedings of the National Academy of Sciences of the United States of America*,
892 *111*(5), E592-600. https://doi.org/10.1073/pnas.1318157111
893 Kwon, O.-J., Zhang, L., & Xin, L. (2016). Stem Cell Antigen-1 Identifies a Distinct Androgen-
894 Independent Murine Prostatic Luminal Cell Lineage with Bipotent Potential. *STEM CELLS*,
895 *34*(1), 191–202. https://doi.org/10.1002/stem.2217
896 Lawson, D. A., Xin, L., Lukacs, R. U., Cheng, D., & Witte, O. N. (2007). Isolation and functional
897 characterization of murine prostate stem cells. *Proceedings of the National Academy of*
898 *Sciences of the United States of America*, *104*(1), 181–186.
899 https://doi.org/10.1073/pnas.0609684104
900 Leong, K. G., Wang, B.-E., Johnson, L., & Gao, W.-Q. (2008). Generation of a prostate from a
901 single adult stem cell. *Nature*, *456*(7223), 804–808.
902 https://doi.org/10.1038/nature07427
903 Lie-A-Ling, M., Mevel, R., Patel, R., Blyth, K., Baena, E., Kouskoff, V., & Lacaud, G. (2020). RUNX1
904 Dosage in Development and Cancer. *Molecules and Cells*, *43*(2), 126–138.
905 https://doi.org/10.14348/molcells.2019.0301
906 Little, G. H., Baniwal, S. K., Adisetiyo, H., Groshen, S., Chimge, N.-O., Kim, S. Y., Khalid, O.,
907 Hawes, D., Jones, J. O., Pinski, J., Schones, D. E., & Frenkel, B. (2014). Differential effects
908 of RUNX2 on the androgen receptor in prostate cancer: Synergistic stimulation of a gene

909 set exemplified by SNAI2 and subsequent invasiveness. *Cancer Research*, *74*(10), 2857–
910 2868. https://doi.org/10.1158/0008-5472.CAN-13-2003
911 Lopes, E. S., Foster, B. A., Donjacour, A. A., & Cunha, G. R. (1996). Initiation of secretory activity
912 of rat prostatic epithelium in organ culture. *Endocrinology*, *137*(10), 4225–4234.
913 https://doi.org/10.1210/endo.137.10.8828481
914 Luche, H., Weber, O., Nageswara Rao, T., Blum, C., & Fehling, H. J. (2007). Faithful activation of
915 an extra-bright red fluorescent protein in 'knock-in' Cre-reporter mice ideally suited for
916 lineage tracing studies. *European Journal of Immunology*, *37*(1), 43–53.
917 https://doi.org/10.1002/eji.200636745
918 Lukacs, R. U., Goldstein, A. S., Lawson, D. A., Cheng, D., & Witte, O. N. (2010). Isolation,
919 cultivation and characterization of adult murine prostate stem cells. *Nature Protocols*,
920 *5*(4), 702–713. https://doi.org/10.1038/nprot.2010.11
921 McAuley, E., Moline, D., VanOpstall, C., Lamperis, S., Brown, R., & Vander Griend, D. J. (2019).
922 Sox2 Expression Marks Castration-Resistant Progenitor Cells in the Adult Murine
923 Prostate. *Stem Cells (Dayton, Ohio)*, *37*(5), 690–700. https://doi.org/10.1002/stem.2987
924 McGinnis, C. S., Patterson, D. M., Winkler, J., Conrad, D. N., Hein, M. Y., Srivastava, V., Hu, J. L.,
925 Murrow, L. M., Weissman, J. S., Werb, Z., Chow, E. D., & Gartner, Z. J. (2019). MULTI-
926 seq: Sample multiplexing for single-cell RNA sequencing using lipid-tagged indices.
927 *Nature Methods*, *16*(7), 619–626. https://doi.org/10.1038/s41592-019-0433-8
928 McInnes, L., Healy, J., & Melville, J. (2018). UMAP: Uniform Manifold Approximation and
929 Projection for Dimension Reduction. *ArXiv:1802.03426 [Cs, Stat]*.
930 http://arxiv.org/abs/1802.03426

931 McNeal, J. E. (1981). The zonal anatomy of the prostate. *The Prostate*, *2*(1), 35–49.
932 https://doi.org/10.1002/pros.2990020105
933 Mevel, R., Draper, J. E., Lie-a-Ling, M., Kouskoff, V., & Lacaud, G. (2019). RUNX transcription
934 factors: Orchestrators of development. *Development*, *146*(17), dev148296.
935 https://doi.org/10.1242/dev.148296
936 Ousset, M., Van Keymeulen, A., Bouvencourt, G., Sharma, N., Achouri, Y., Simons, B. D., &
937 Blanpain, C. (2012). Multipotent and unipotent progenitors contribute to prostate
938 postnatal development. *Nature Cell Biology*, *14*(11), 1131–1138.
939 https://doi.org/10.1038/ncb2600
940 Pignon, J.-C., Grisanzio, C., Geng, Y., Song, J., Shivdasani, R. A., & Signoretti, S. (2013). P63-
941 expressing cells are the stem cells of developing prostate, bladder, and colorectal
942 epithelia. *Proceedings of the National Academy of Sciences of the United States of*
943 *America*, *110*(20), 8105–8110. https://doi.org/10.1073/pnas.1221216110
944 Planagumà, J., Díaz-Fuertes, M., Gil-Moreno, A., Abal, M., Monge, M., García, A., Baró, T.,
945 Thomson, T. M., Xercavins, J., Alameda, F., & Reventós, J. (2004). A differential gene
946 expression profile reveals overexpression of RUNX1/AML1 in invasive endometrioid
947 carcinoma. *Cancer Research*, *64*(24), 8846–8853. https://doi.org/10.1158/0008-
948 5472.CAN-04-2066
949 Planagumà, J., Gonzalez, M., Doll, A., Monge, M., Gil-Moreno, A., Baró, T., García, A., Xercavins,
950 J., Alameda, F., Abal, M., & Reventós, J. (2006). The up-regulation profiles of
951 p21WAF1/CIP1 and RUNX1/AML1 correlate with myometrial infiltration in endometrioid

952 endometrial carcinoma. *Human Pathology*, *37*(8), 1050–1057.
953 https://doi.org/10.1016/j.humpath.2006.03.007
954 Richardson, G. D., Robson, C. N., Lang, S. H., Neal, D. E., Maitland, N. J., & Collins, A. T. (2004).
955 CD133, a novel marker for human prostatic epithelial stem cells. *Journal of Cell Science*,
956 *117*(16), 3539–3545. https://doi.org/10.1242/jcs.01222
957 Riggio, A. I., & Blyth, K. (2017). The enigmatic role of RUNX1 in female-related cancers—Current
958 knowledge & future perspectives. *The FEBS Journal*, *284*(15), 2345–2362.
959 https://doi.org/10.1111/febs.14059
960 Samokhvalov, I. M., Samokhvalova, N. I., & Nishikawa, S. (2007). Cell tracing shows the
961 contribution of the yolk sac to adult haematopoiesis. *Nature*, *446*(7139), 1056–1061.
962 https://doi.org/10.1038/nature05725
963 Scheitz, C. J. F., Lee, T. S., McDermitt, D. J., & Tumbar, T. (2012). Defining a tissue stem cell-
964 driven Runx1/Stat3 signalling axis in epithelial cancer. *The EMBO Journal*, *31*(21), 4124–
965 4139. https://doi.org/10.1038/emboj.2012.270
966 Scheitz, C. J. F., & Tumbar, T. (2013). New insights into the role of Runx1 in epithelial stem cell
967 biology and pathology. *Journal of Cellular Biochemistry*, *114*(5), 985–993.
968 https://doi.org/10.1002/jcb.24453
969 Shen, M. M., & Abate-Shen, C. (2010). Molecular genetics of prostate cancer: New prospects for
970 old challenges. *Genes & Development*, *24*(18), 1967–2000.
971 https://doi.org/10.1101/gad.1965810

972 Sroczynska, P., Lancrin, C., Kouskoff, V., & Lacaud, G. (2009). The differential activities of Runx1
973 promoters define milestones during embryonic hematopoiesis. *Blood*, *114*(26), 5279–
974 5289. https://doi.org/10.1182/blood-2009-05-222307
975 Sugimura, Y., Cunha, G. R., & Donjacour, A. A. (1986a). Morphogenesis of ductal networks in the
976 mouse prostate. *Biology of Reproduction*, *34*(5), 961–971.
977 https://doi.org/10.1095/biolreprod34.5.961
978 Sugimura, Y., Cunha, G. R., & Donjacour, A. A. (1986b). Morphological and histological study of
979 castration-induced degeneration and androgen-induced regeneration in the mouse
980 prostate. *Biology of Reproduction*, *34*(5), 973–983.
981 Takayama, K., Suzuki, T., Tsutsumi, S., Fujimura, T., Urano, T., Takahashi, S., Homma, Y.,
982 Aburatani, H., & Inoue, S. (2015). RUNX1, an androgen- and EZH2-regulated gene, has
983 differential roles in AR-dependent and -independent prostate cancer. *Oncotarget*, *6*(4),
984 2263–2276. https://doi.org/10.18632/oncotarget.2949
985 Thambyrajah, R., Mazan, M., Patel, R., Moignard, V., Stefanska, M., Marinopoulou, E., Li, Y.,
986 Lancrin, C., Clapes, T., Möröy, T., Robin, C., Miller, C., Cowley, S., Göttgens, B., Kouskoff,
987 V., & Lacaud, G. (2016). GFI1 proteins orchestrate the emergence of haematopoietic
988 stem cells through recruitment of LSD1. *Nature Cell Biology*, *18*(1), 21–32.
989 https://doi.org/10.1038/ncb3276
990 Tika, E., Ousset, M., Dannau, A., & Blanpain, C. (2019). Spatiotemporal regulation of
991 multipotency during prostate development. *Development*, dev.180224.
992 https://doi.org/10.1242/dev.180224

993 Tirosh, I., Izar, B., Prakadan, S. M., Wadsworth, M. H., Treacy, D., Trombetta, J. J., Rotem, A.,
994 Rodman, C., Lian, C., Murphy, G., Fallahi-Sichani, M., Dutton-Regester, K., Lin, J.-R.,
995 Cohen, O., Shah, P., Lu, D., Genshaft, A. S., Hughes, T. K., Ziegler, C. G. K., … Garraway, L.
996 A. (2016). Dissecting the multicellular ecosystem of metastatic melanoma by single-cell
997 RNA-seq. *Science*, *352*(6282), 189–196. https://doi.org/10.1126/science.aad0501
998 Toivanen, R., Mohan, A., & Shen, M. M. (2016). Basal Progenitors Contribute to Repair of the
999 Prostate Epithelium Following Induced Luminal Anoikis. *Stem Cell Reports*, *0*(0).
1000 https://doi.org/10.1016/j.stemcr.2016.03.007
1001 Toivanen, R., & Shen, M. M. (2017). Prostate organogenesis: Tissue induction, hormonal
1002 regulation and cell type specification. *Development (Cambridge, England)*, *144*(8), 1382–
1003 1398. https://doi.org/10.1242/dev.148270
1004 Tsujimura, A., Koikawa, Y., Salm, S., Takao, T., Coetzee, S., Moscatelli, D., Shapiro, E., Lepor, H.,
1005 Sun, T.-T., & Wilson, E. L. (2002). Proximal location of mouse prostate epithelial stem
1006 cells. *The Journal of Cell Biology*, *157*(7), 1257–1265.
1007 https://doi.org/10.1083/jcb.200202067
1008 van Bragt, M. P. A., Hu, X., Xie, Y., & Li, Z. (2014). RUNX1, a transcription factor mutated in
1009 breast cancer, controls the fate of ER-positive mammary luminal cells. *ELife*, *3*, e03881.
1010 https://doi.org/10.7554/eLife.03881
1011 Wang, B., Wang, X., Long, J. E., Eastham-Anderson, J., Firestein, R., & Junttila, M. R. (2015).
1012 Castration-Resistant Lgr5+ Cells Are Long-Lived Stem Cells Required for Prostatic
1013 Regeneration. *Stem Cell Reports*, *4*(5), 768–779.
1014 https://doi.org/10.1016/j.stemcr.2015.04.003

1015 Wang, X., Kruithof-de Julio, M., Economides, K. D., Walker, D., Yu, H., Halili, M. V., Hu, Y.-P.,
1016 Price, S. M., Abate-Shen, C., & Shen, M. M. (2009). A luminal epithelial stem cell that is a
1017 cell of origin for prostate cancer. *Nature*, *461*(7263), 495–500.
1018 https://doi.org/10.1038/nature08361
1019 Wang, X.-D., Wang, B.-E., Soriano, R., Zha, J., Zhang, Z., Modrusan, Z., Cunha, G. R., & Gao, W.-
1020 Q. (2007). Expression profiling of the mouse prostate after castration and hormone
1021 replacement: Implication of H-cadherin in prostate tumorigenesis. *Differentiation;*
1022 *Research in Biological Diversity*, *75*(3), 219–234. https://doi.org/10.1111/j.1432-
1023 0436.2006.00135.x
1024 Wang, Y., Hayward, S., Cao, M., Thayer, K., & Cunha, G. (2001). Cell differentiation lineage in the
1025 prostate. *Differentiation; Research in Biological Diversity*, *68*(4–5), 270–279.
1026 Wolf, F. A., Hamey, F. K., Plass, M., Solana, J., Dahlin, J. S., Göttgens, B., Rajewsky, N., Simon, L.,
1027 & Theis, F. J. (2019). PAGA: Graph abstraction reconciles clustering with trajectory
1028 inference through a topology preserving map of single cells. *Genome Biology*, *20*(1), 59.
1029 https://doi.org/10.1186/s13059-019-1663-x
1030 Xin, L., Lawson, D. A., & Witte, O. N. (2005). The Sca-1 cell surface marker enriches for a
1031 prostate-regenerating cell subpopulation that can initiate prostate tumorigenesis.
1032 *Proceedings of the National Academy of Sciences of the United States of America*,
1033 *102*(19), 6942–6947. https://doi.org/10.1073/pnas.0502320102
1034 Yokomizo, T., Yamada-Inagawa, T., Yzaguirre, A. D., Chen, M. J., Speck, N. A., & Dzierzak, E.
1035 (2012). Whole-mount three-dimensional imaging of internally localized immunostained

1036 cells within mouse embryos. *Nature Protocols*, *7*(3), 421–431.
1037 https://doi.org/10.1038/nprot.2011.441
1038 Yoo, Y. A., Roh, M., Naseem, A. F., Lysy, B., Desouki, M. M., Unno, K., & Abdulkadir, S. A. (2016).
1039 Bmi1 marks distinct castration-resistant luminal progenitor cells competent for prostate
1040 regeneration and tumour initiation. *Nature Communications*, *7*, 12943.
1041 https://doi.org/10.1038/ncomms12943
1042 Zhang, D., Zhao, S., Li, X., Kirk, J. S., & Tang, D. G. (2018). Prostate Luminal Progenitor Cells in
1043 Development and Cancer. *Trends in Cancer*, *4*(11), 769–783.
1044 https://doi.org/10.1016/j.trecan.2018.09.003
1045

1046 **TABLES**

1047 **Table 1. List of primary antibodies used for immunohistochemistry**

Target	Provider	Catalog Number	Raised specie
RUNX1	Cell Signalling	8529	Rabbit
NKX3.1	Athenaes	AES-0314	Rabbit
CDH1	Thermo Fischer	AF748	Goat
TP63	Cell Signalling	M3562	Rabbit
K5	Abcam	ab52635	Rabbit
K8	Abcam	ab53280	Rabbit
K4	Abcam	Ab9004	Mouse
LY6D	Proteintech	17361-1-AP	Rabbit
TROP-2	R&D	AF1122	Goat
BrdU	Abcam	ab6326	Rat
Ki67	Abcam	ab15580	Rabbit
RFP	Rockland	600-402-379	Rabbit
RFP	MBL	PM005	Rabbit
GFP	MBL	598	Rabbit

1048

1049

1050

1051

1052

1053 **Table 2. List of primary antibodies used for immunohistochemistry**

Antibody	Provider	Catalog Number
EnVision+/HRP Anti-Rabbit	Dako (Agilent)	K4003
EnVision+/HRP Anti-Rabbit	Dako (Agilent)	K4001
ImmPRESS HRP Anti-Goat	Vector Laboratories	MP-7405
ImmPRESS HRP Anti-Rat	Vector Laboratories	MP-7444
Donkey anti-Goat IgG 647	ThermoFischer Scientific	A-21447

1054

1055 **Table 3. List of antibodies used for Fluorescence-Activated Cell Sorting (FACS)**

Target	Provider	Catalog Number	Clone	Fluorophore
CD16/32	Biolegend	101301	93	none (Fc block)
CD45	Biolegend	62-0451-82	30-F11	SB436
EPCAM	Biolegend	118225	G8.8	BV421
EPCAM	Biolegend	118214	G8.8	APC
CD49f	Biolegend	313606	GoH3	FITC
CD49f	Biolegend	313616	GoH3	APC
CD24	BD Biosciences	744470	M1/69	BV786

1056

1057 ## SUPPLEMENTARY FILES

1058 **Supplementary file 1. Quality control metrics and metadata of scRNAseq experiments**

1059 **Supplementary file 2. Genes differentially expressed between adult clusters**

1060 **Supplementary file 3. Genes differentially expressed in intact versus castrated Lum-D cells**

1061 **Supplementary file 4. Genes differentially expressed between UGS explants clusters**

1062 **Supplementary file 5. Gene lists used for the analysis of gene set activity**

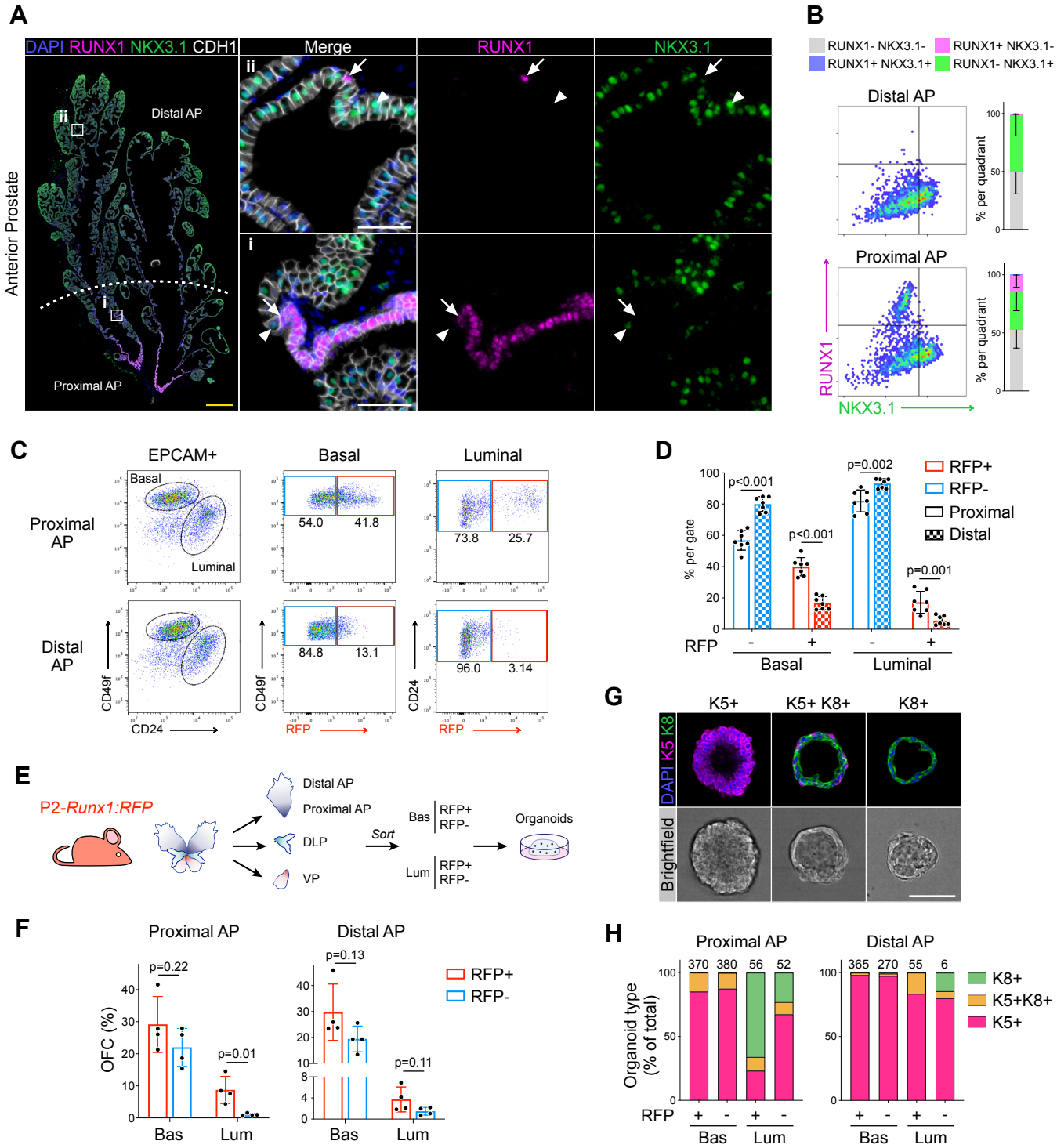

Figure 1. RUNX1 marks a subpopulation of mouse proximal prostate luminal cells (PLCs).

(**A**) Co-immunostaining of RUNX1, NKX3.1, CDH1 in the mouse Anterior Prostate (AP). Higher magnification images of (i) proximal AP and (ii) distal AP are shown. Arrows indicate RUNX1$^+$ NKX3.1$^-$ cells, arrowheads show RUNX1$^-$ NKX3.1$^+$ cells. Scale bars: 500µm (yellow) and 50µm (white). (**B**) Quantification of RUNX1 and NKX3.1 nuclear intensity (log10) in CDH1$^+$ epithelial cells by QBIC in proximal and distal AP. *n* = 6-8 mice. (**C, D**) Flow-cytometry analysis of P2-*Runx1*:RFP mice, and corresponding quantification of the percentages of RFP$^+$ and RFP$^-$ cells in the basal and luminal fractions of the proximal and distal AP. *n* = 7 mice. (**E**) Experimental strategy to grow organoids from sorted RFP$^+$ and RFP$^-$ cells from the basal (CD49f^{high}) and luminal (CD24^{high}) lineages of P2-*Runx1*:RFP mouse reporters. (**F**) Organoid Forming Capacity (OFC) of RFP$^+$ and RFP$^-$ basal and luminal sorted cells after 7 days in culture. *n* = 4 mice. (**G**) Whole-mount immunostaining of unipotent K5$^+$, unipotent K8$^+$ or multipotent K5$^+$ K8$^+$ organoids. Scale bar: 50µm. (**H**) Quantification of the type of organoids characterized by whole-mount immunostaining, as in (**G**). Numbers of organoids quantified are shown above the graph. *n* = 2 mice per group.

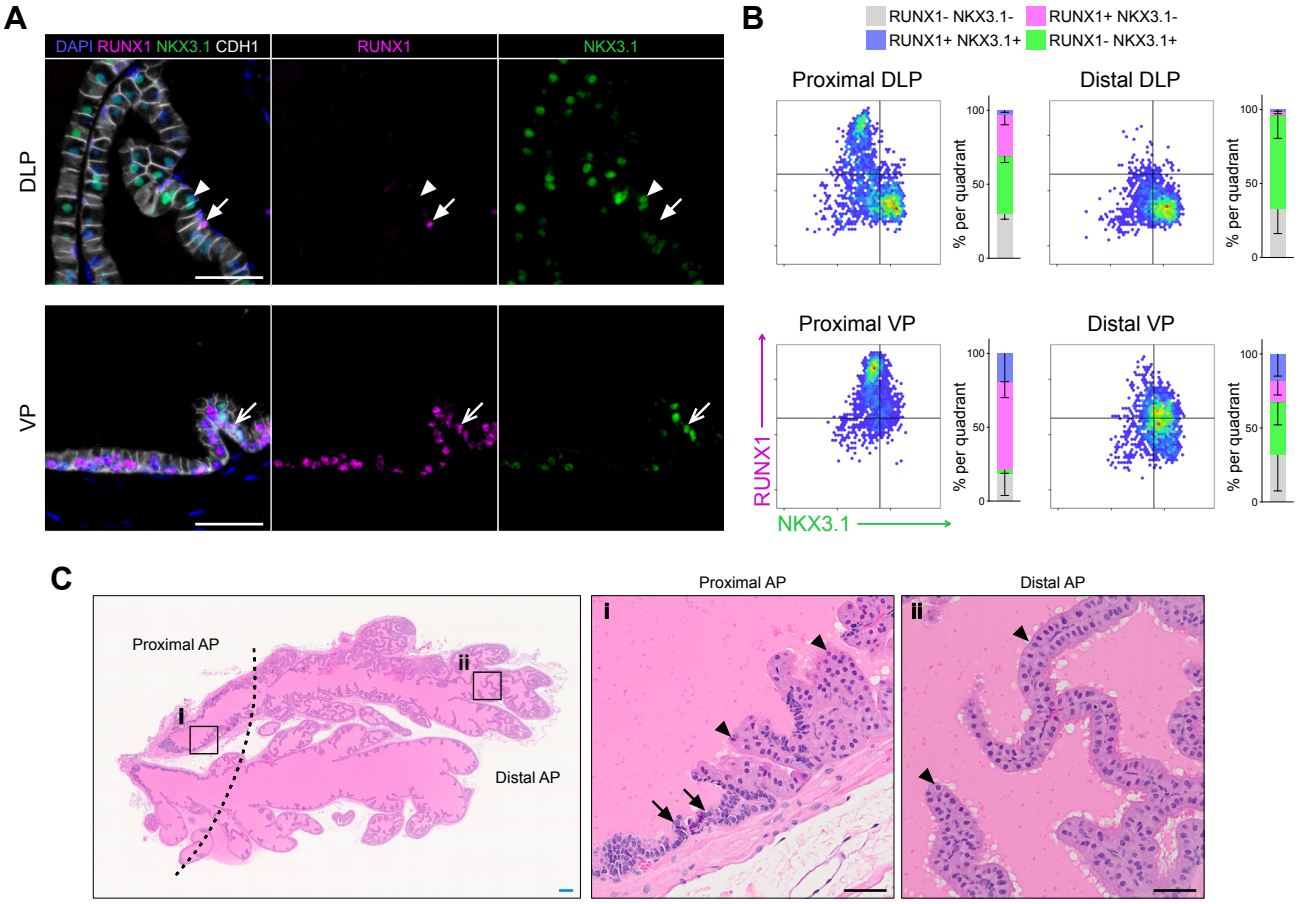

Figure 1—figure supplement 1. RUNX1 is enriched in the mouse prostate epithelium.

(**A**) Co-immunostaining of RUNX1, NKX3.1, CDH1 in the mouse DLP (top) and VP (bottom). Closed arrows indicate RUNX1^{+} NKX3.1^{-} cells, chevron arrows indicate rare RUNX1^{+} NKX3.1^{+} cells, arrowheads show RUNX1^{-} NKX3.1^{+} cells. Scale bars: 50μm. (**B**) Quantification of RUNX1 and NKX3.1 nuclear intensity (log10) in CDH1+ epithelial cells by QBIC in proximal DLP (*n* = 3), distal DLP (*n* = 8), proximal VP (*n* = 3) and distal VP (*n* = 8). (**C**) H&E staining of the mouse AP. Higher magnification images of (i) proximal AP and (ii) distal regions are shown. Arrows show typical proximal luminal cells with condensed nuclei and cytoplasm, arrowheads show typical distal secretory luminal cells with enlarged cytoplasm and strong pink eosinophilic staining. Scale bars: 200μm (blue) and 50μm (black).

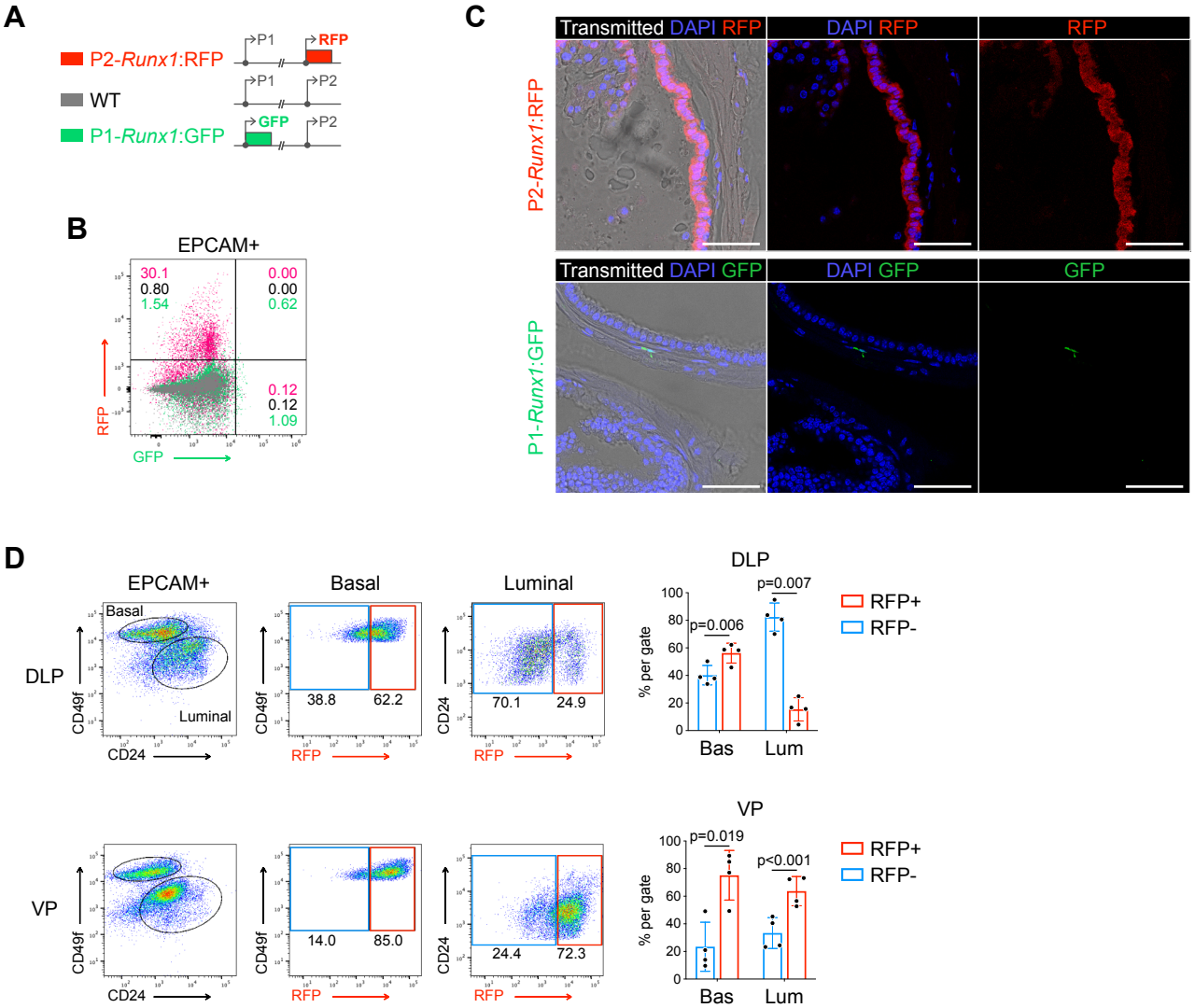

Figure 1—figure supplement 2. *Runx1* expression is mediated by the P2 promoter in the mouse prostate epithelium.

(**A**) Schematic diagrams of the P2-*Runx1*:RFP reporter allele (top), Runx1 WT allele (middle), and P1-*Runx1*:GFP reporter allele (bottom). In P2-*Runx1*:RFP or P1-*Runx1*:GFP mice, expression of RFP or GFP is directed by *Runx1* proximal P2 or distal P1 promoter respectively. WT *Runx1* expression is directed by the remaining WT allele. (**B**) Flow-cytometry analysis of the epithelial EPCAM$^+$ fraction of WT, P2-*Runx1*:RFP and P1-*Runx1*:GFP mice. Percentages are indicated in each quadrant gates. (**C**) Confocal images indicating P2-*Runx1*:RFP signal in the glandular epithelium (top), while P1-*Runx1*:GFP (bottom) activity is detected in the surrounding stroma. Scale bar: 50μm. (**D**) Flow-cytometry analysis of P2-*Runx1*:RFP mice, and corresponding quantification of the percentages of RFP$^+$ and RFP$^-$ cells in the basal and luminal fractions of DLP (n = 4 mice) and VP (n = 4 mice) lobes.

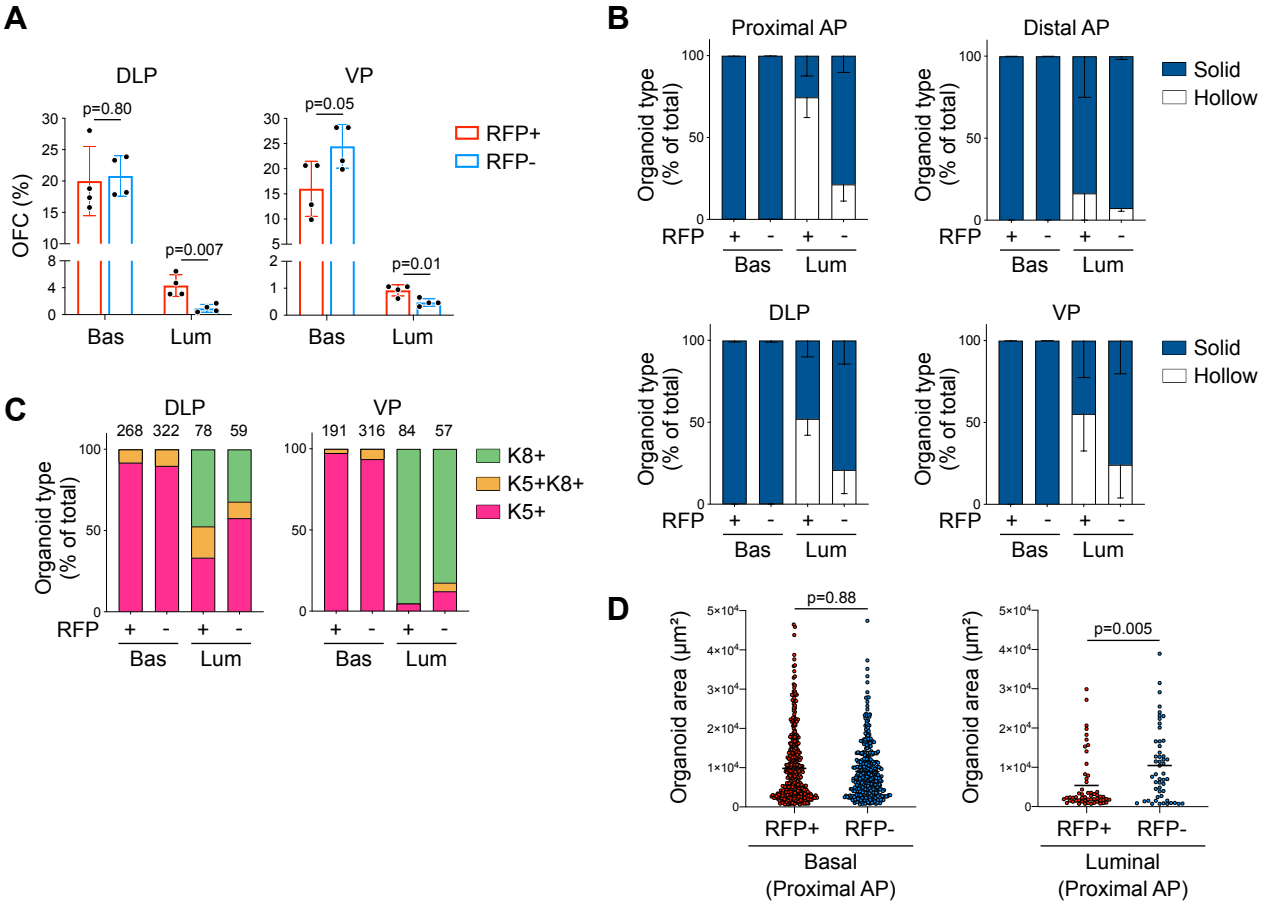

Figure 1—figure supplement 3. Characterization of P2-*Runx1*:RFP derived mouse prostate organoids.

(**A**) Organoid Forming Capacity (OFC) of RFP$^+$ and RFP$^-$ basal and luminal sorted cells from DLP (left) and VP (right) cultured for 7 days. *n* = 4 independent experiments. (**B**) Quantification of organoid morphologies determined by brightfield assessment. *n* = 4 mice. (**C**) Quantification of the type of organoids (pink: unipotent K5$^+$, green: unipotent K8$^+$, orange: multipotent K5$^+$ K8$^+$ organoids) characterized by whole-mount immunostaining. *n* = 2 mice. (**D**) Quantification of the organoid area estimated from maximum projection of stacked images from basal (left) and luminal (right) fractions of the proximal AP. Numbers of organoids quantified are shown above the graph. *n* = 2 mice.

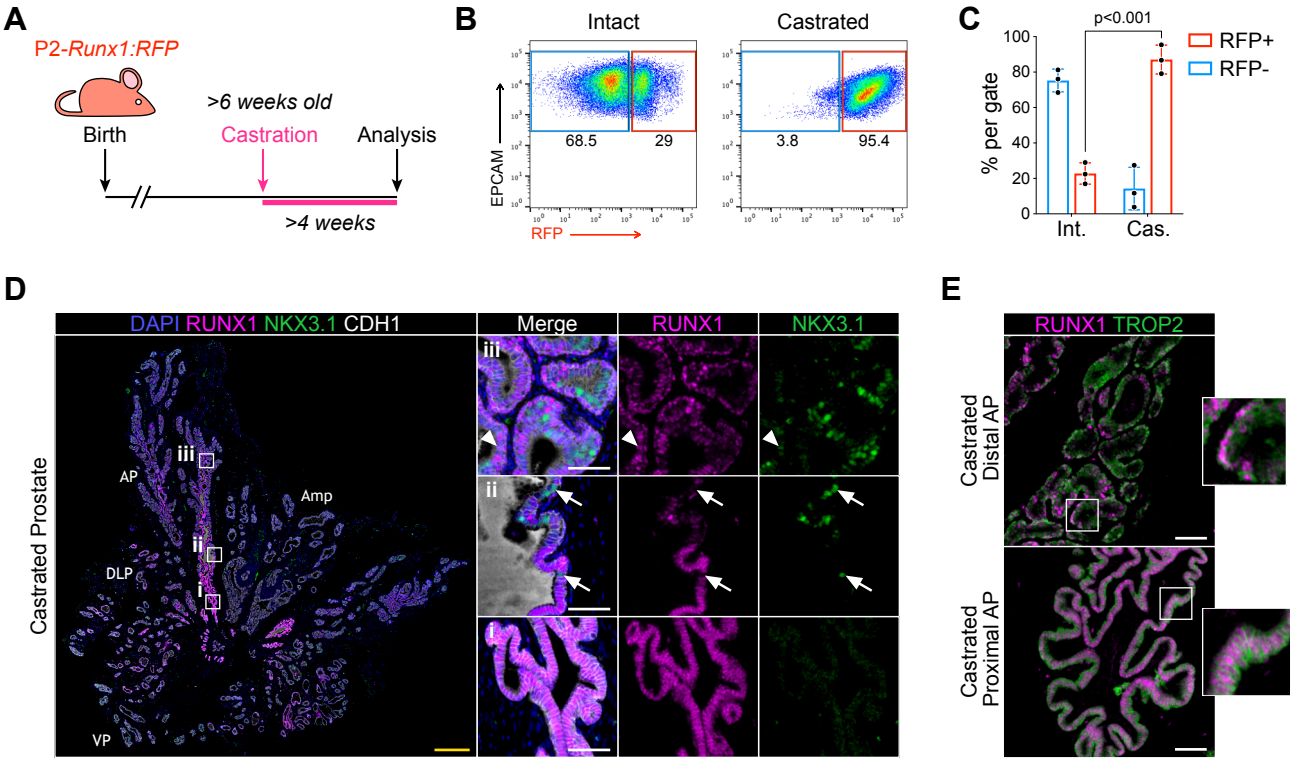

Figure 2. RUNX1 expressing cells are enriched in the castrated prostate epithelium.

(**A**) P2-*Runx1*:RFP reporter mice were surgically castrated between 6 to 12 weeks of age and analyzed at least 4 weeks post-castration. (**B**, **C**) Flow-cytometry analysis and corresponding quantification of the proportion of RFP$^+$ and RFP$^-$ cells in the EPCAM$^+$ fraction of intact and castrated prostates of P2-*Runx1*:RFP mice. *n* = 3 mice per group. Int: Intact, Cas: Castrated. (**D**) Co-immunostaining of RUNX1, NKX3.1, CDH1 in the castrated wild-type mouse prostate. Higher magnification images of (i) proximal, (ii) intermediate and (iii) distal AP are shown. Arrows indicate cells RUNX1$^-$ NKX3.1$^+$ cells, arrowheads show luminal cell co-stained for RUNX1 and NKX3.1. Amp: ampullary gland. Scale bars: 500µm (yellow) and 50µm (white). Int: Intact, Cas: Castrated. (**E**) Co-immunostaining of RUNX1 and TROP2 showing colocalization of the 2 markers in both proximal (bottom) and distal (top) castrated AP. Scale bars: 50µm (white).

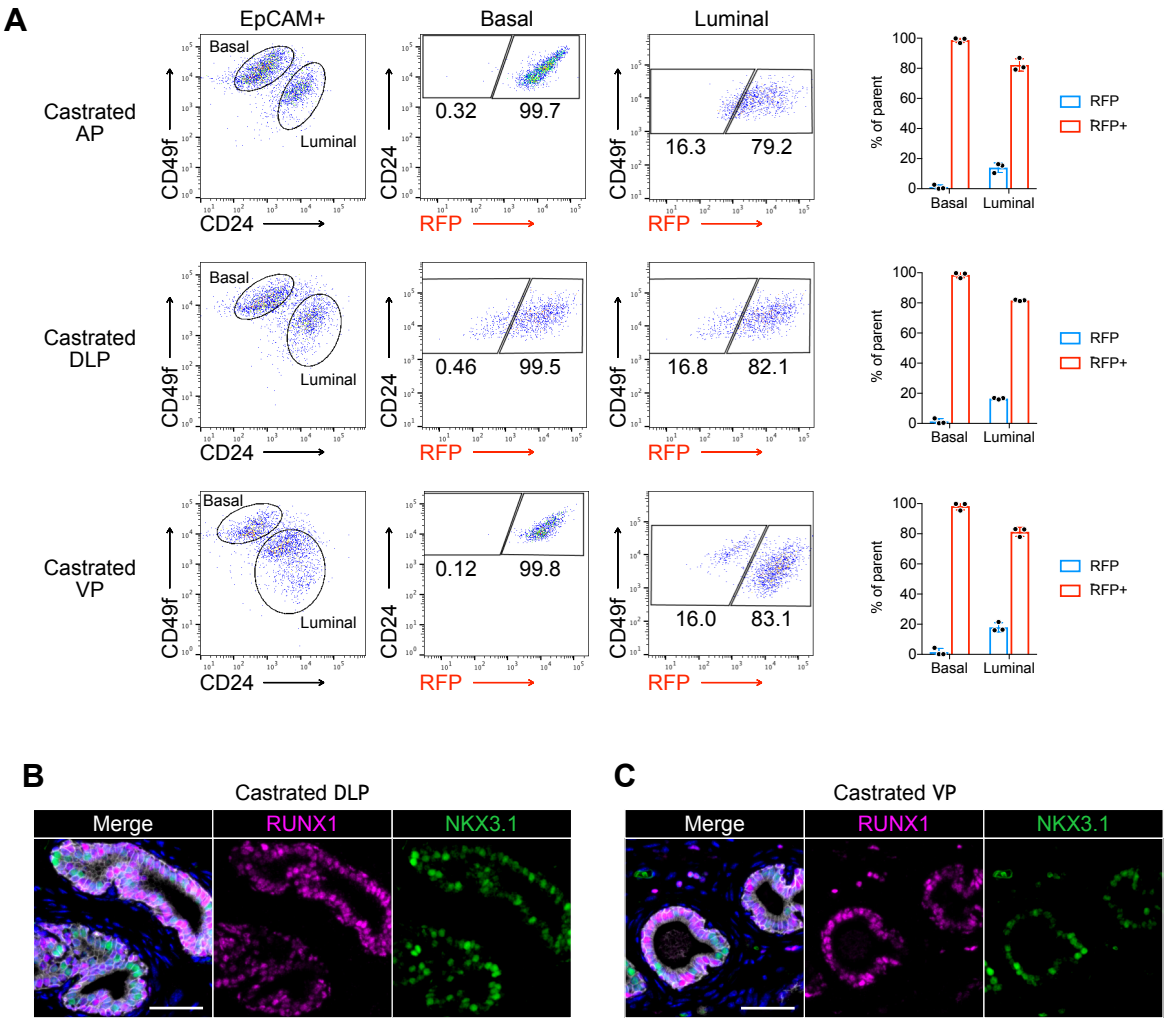

Figure 2—figure supplement 4. Characterization of RUNX1 expression in the castrated mouse prostate.

(**A**) Flow cytometry analysis and corresponding quantifications of the basal and luminal EPCAM^{+} fraction from AP, DLP and VP lobes of castrated P2-*Runx1*:RFP mice (*n* = 3). (**B, C**) Co-immunostaining of RUNX1, NKX3.1, CDH1 in castrated DLP (**B**) and VP (**C**) lobes. Scale bars: 50μm (white).

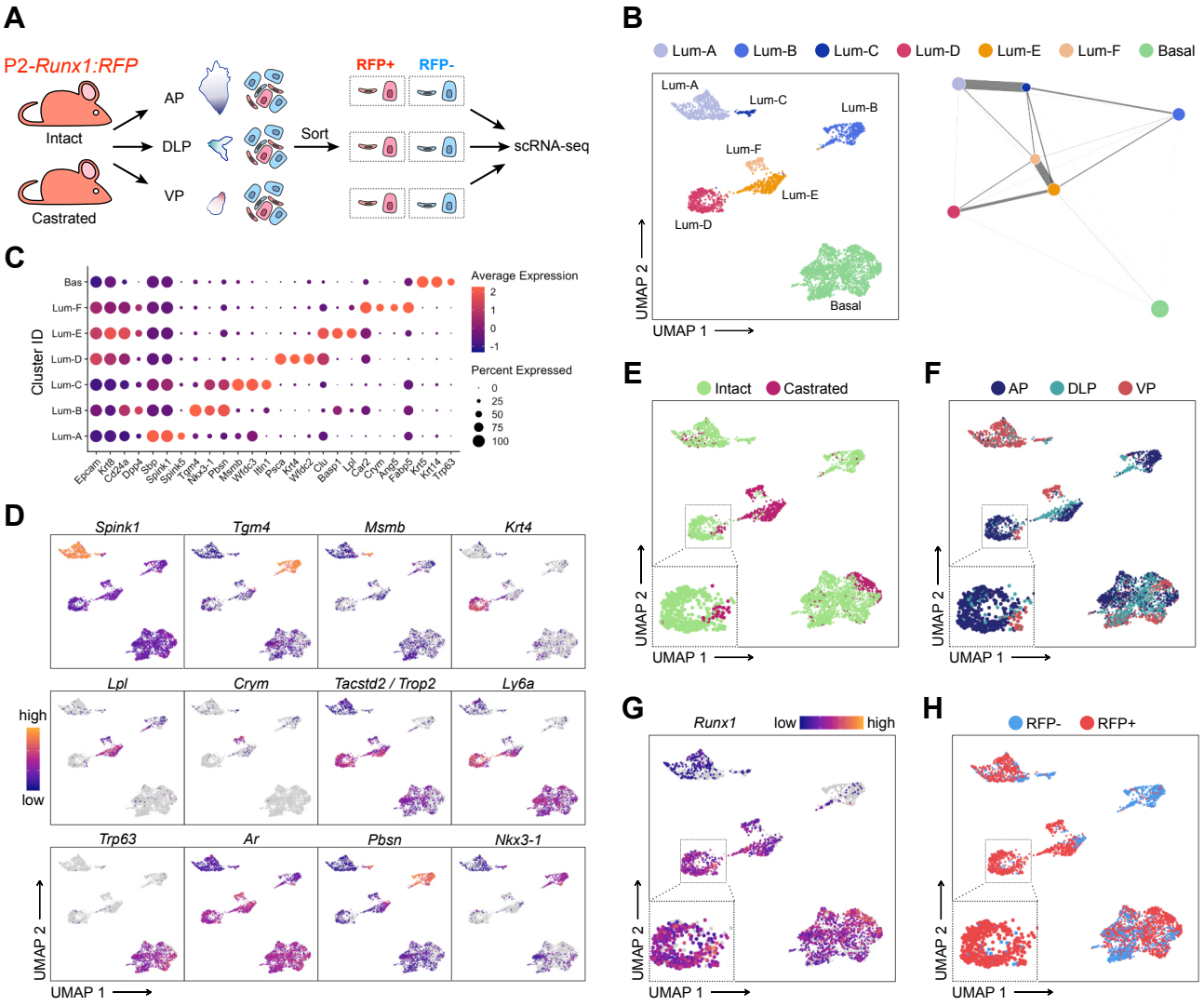

Figure 3. scRNA-seq profiling of intact and castrated *Runx1*⁺ cells reveals transcriptomic similarity between proximal luminal cells and castration-resistant cells.

(**A**) Experimental strategy for scRNA-seq on RFP⁺ and RFP⁻ cells individually dissected lobes of intact and castrated prostates isolated from P2-*Runx1*:RFP reporter mice. (**B**) UMAP visualization (left) and graph-abstracted representation (PAGA, right) of prostate epithelial cells (*n* = 3,825 cells from 3 independent experiments). Colors represent different clusters. In PAGA, clusters are linked by weighted edges that represent a statistical measure of connectivity. (**C**) Dot plot showing the expression of selected marker genes associated with each cluster. (**D-H**) UMAP visualization of prostate epithelial cells. Cells in **D** and **G** are colored by a gradient of log-normalized expression levels for each gene indicated. Cell colors in **E** represent the treatment of origin (intact, castrated), in **F** individual lobes of origin (AP, DLP, VP), and in (**H**) RFP FACS gate of origin (RFP⁺, RFP⁻).

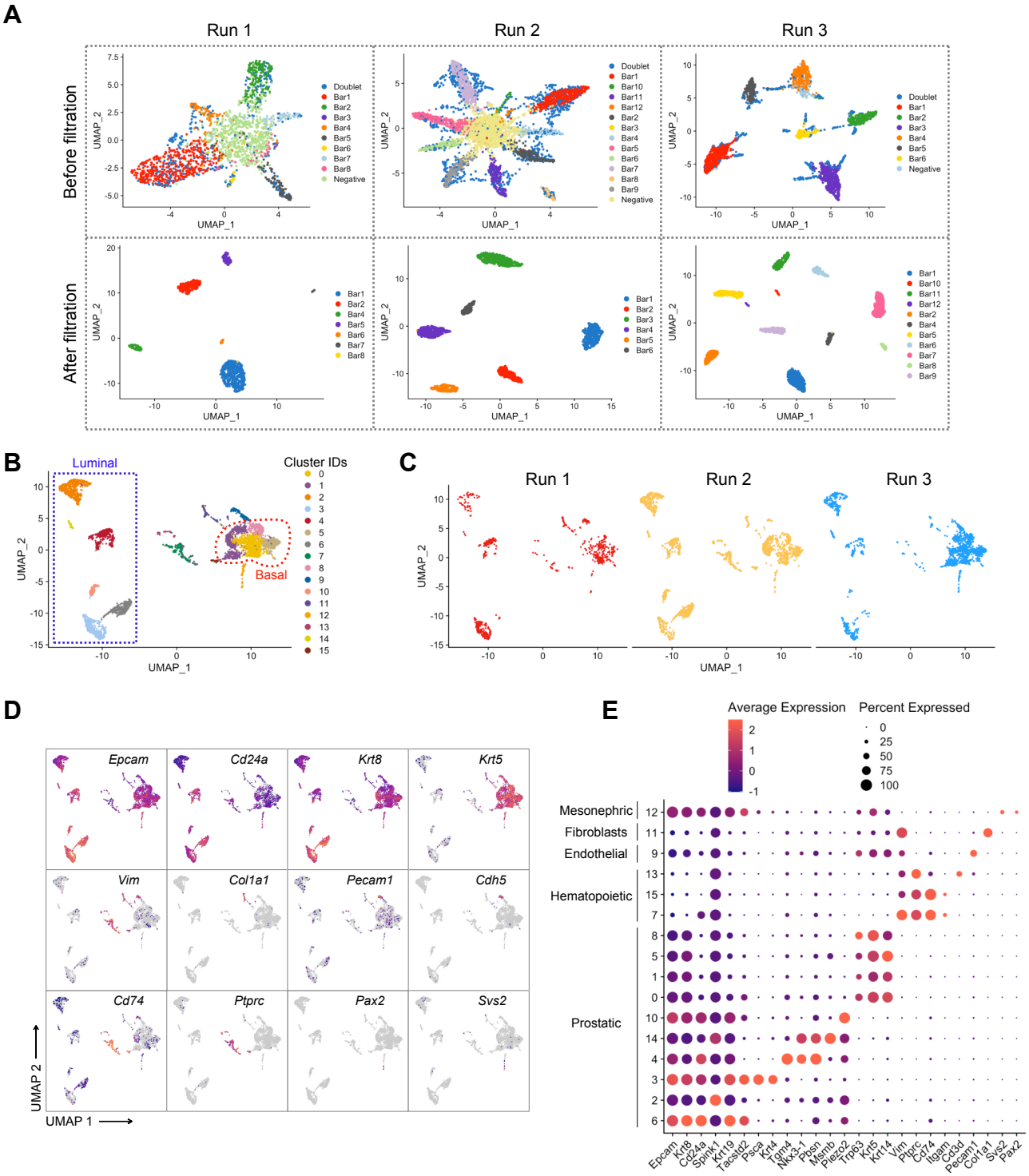

Figure 3—figure supplement 5. Pre-processing of the scRNA-seq dataset of adult intact and castrated mouse prostates.

(**A**) UMAP visualization in MULTI-seq barcodes space for each independent experiment (Run1: left, Run2: middle, Run 3: right) before (top) and after (bottom) quality control and barcode filtration (see Methods for details). (**B**) UMAP visualization of the integrated batch-corrected dataset (n = 4,499 cells from 3 independent experiments). Colors represent different clusters. (**C**) UMAP visualization of the integrated batch-corrected dataset split and colored by individual experiment (Run1: left, Run2: middle, Run 3: right). (**D**, **E**) Example key marker genes used for cell type characterization. (**D**) UMAP visualization of the integrated batch-corrected dataset. Cells are colored by a gradient of log-normalized expression levels for each gene indicated. (**E**) Dot plot showing the expression of selected marker genes associated with each cluster. Cells corresponding to the prostatic clusters were kept for downstream analyses.

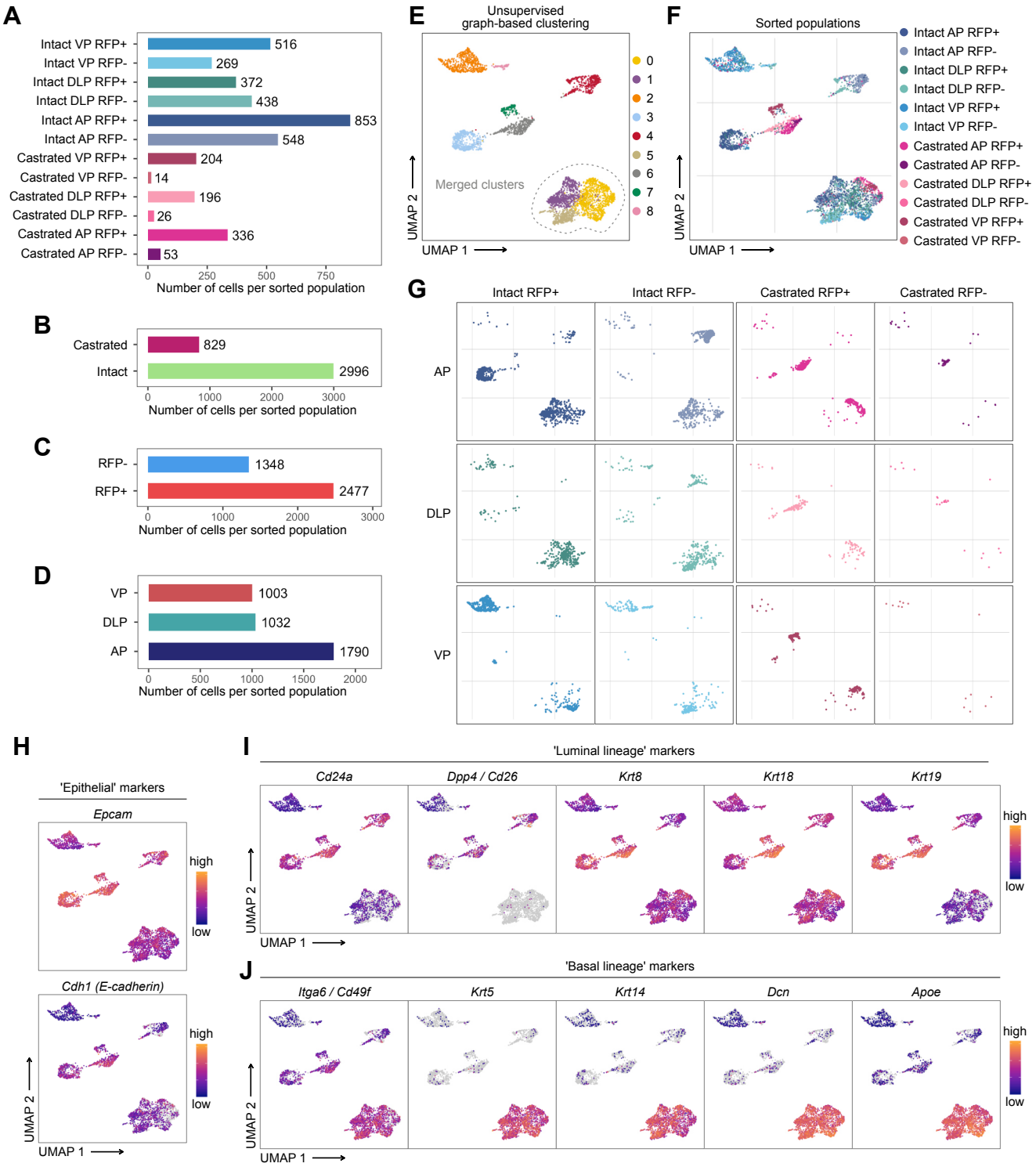

Figure 3—figure supplement 6. Characterization of the scRNA-seq prostate epithelial subset.

(**A**-**D**) Number of cells present in the prostate epithelial subset. In **A** colors correspond to phenotypic sorted populations, in **B** treatment of origin, in **C** RFP FACS gate of origin, in **D** individual lobes. (**E, G**) UMAP visualization of prostate epithelial cells. Cells in **E** are colored by clusters. Clusters 0, 1 and 5 were merged together. In **F** and **G** colors represent phenotypic sorted populations. (**H-J**) Cells are colored by a gradient of log-normalized expression levels for each gene. Canonical epithelial markers are shown in **H**, luminal lineage markers in **I**, and basal lineage markers in **J**.

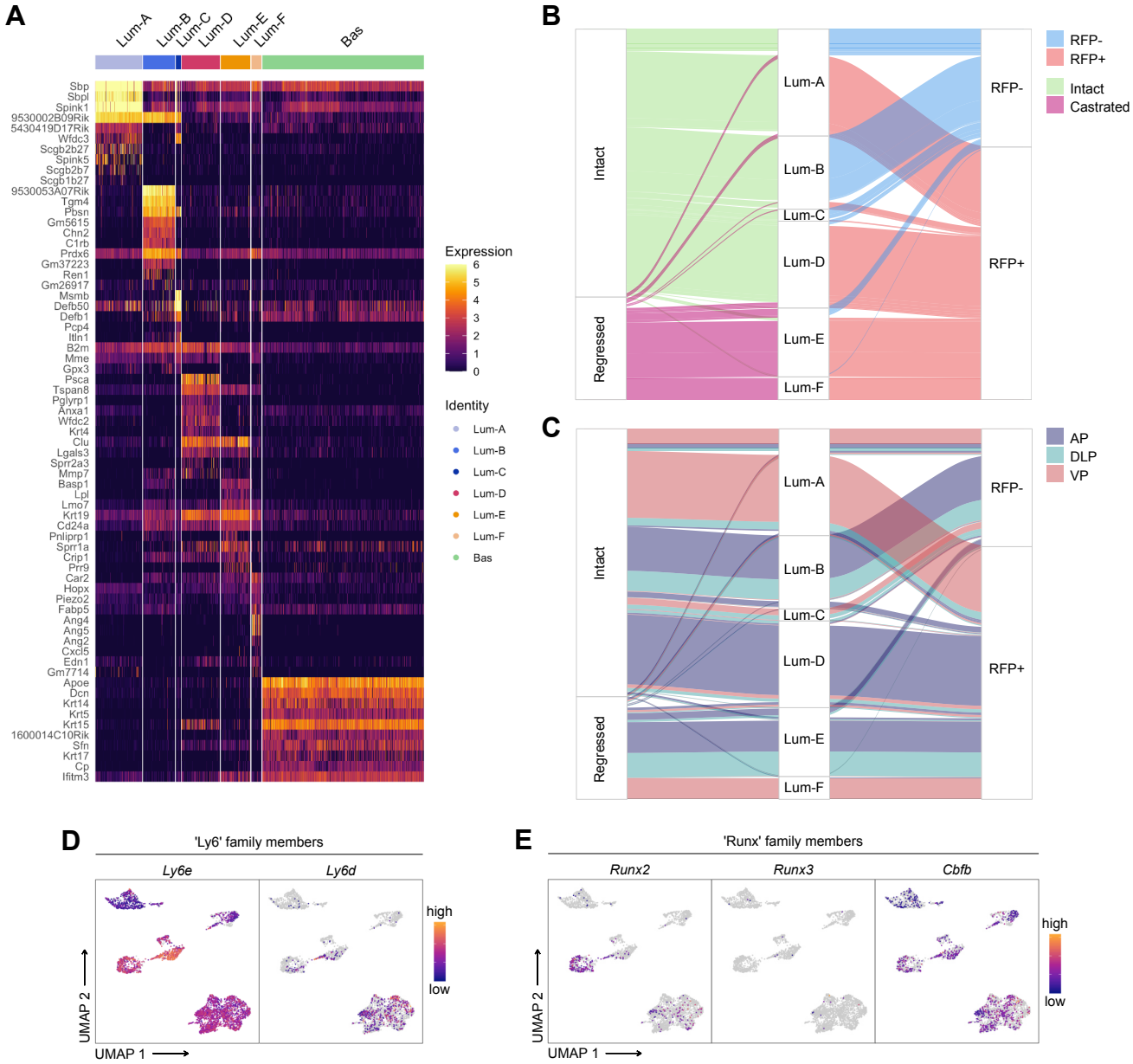

Figure 3—figure supplement 7. Characterization of the scRNA-seq prostate epithelial dataset.

(**A**) Heatmap of the 10 most differentially upregulated genes per cluster. (**B**, **C**) Sankey diagrams summarizing the proportion of cells and between phenotypic groups. (**D**, **E**) Cells are colored by a gradient of log-normalized expression levels for each gene. (**D**) shows the expression of Ly6 family members, and in **E** RUNX family members are shown.

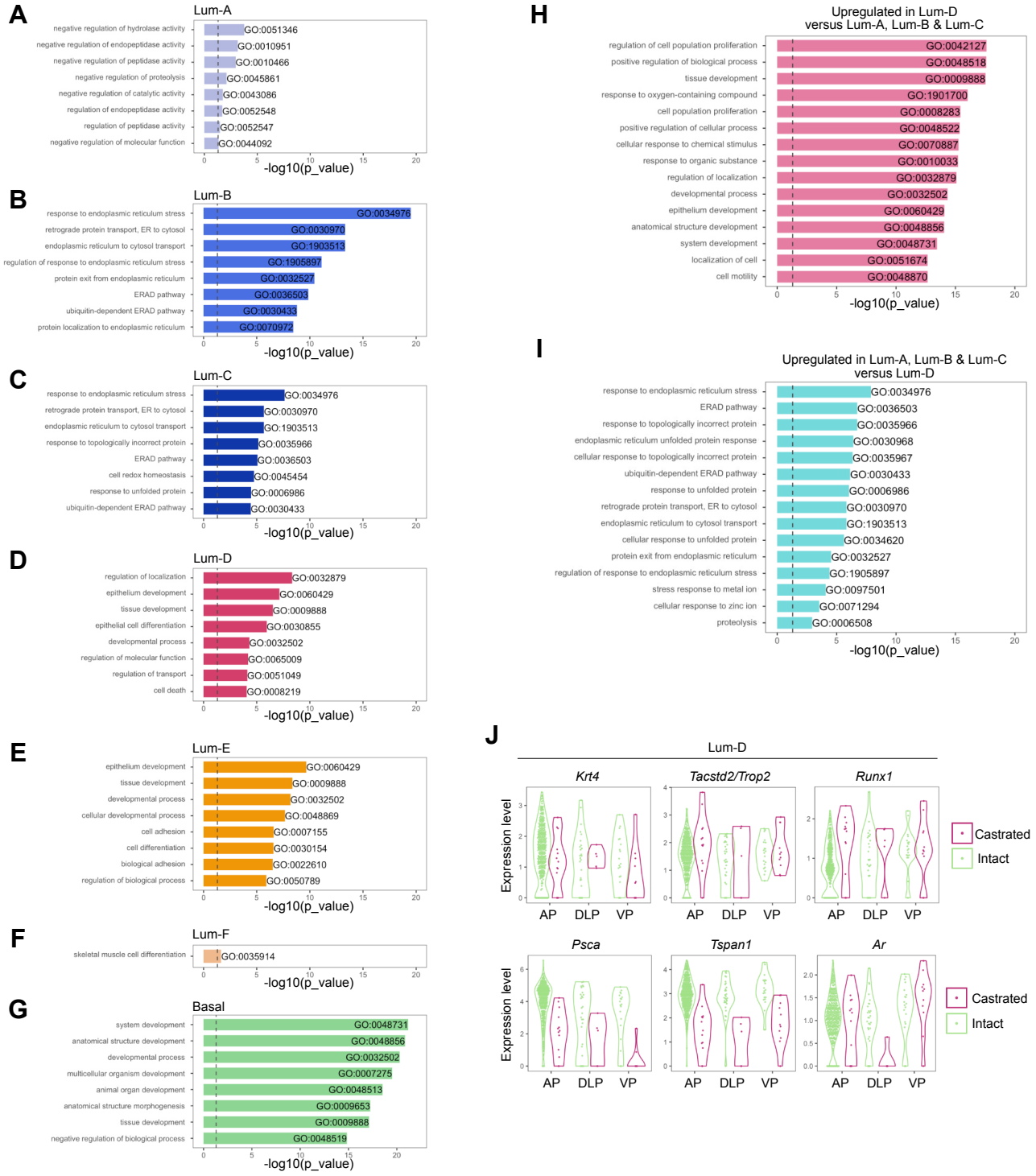

Figure 3—figure supplement 8. Gene Ontology and differential expression analysis within the scRNA-seq prostate epithelial dataset.

Bar plots of the 8 most significantly (g:Profiler adjusted p-value < 0.05) enriched gene ontology (GO) terms (GO:BP, Biological Processes) using the list of differentially upregulated genes specific to (**A**) Lum-A, (**B**) Lum-B, (**C**) Lum-C, (**D**) Lum-D, (**E**) Lum-E, (**F**) Lum-F, and (**G**) Basal clusters. (**H, I**) 15 most enriched GO terms (g:Profiler adjusted p-value < 0.05) for genes upregulated in the Lum-D cluster against combined Lum-A, Lum-B and Lum-C clusters in **H**. Results of the opposite comparison are shown in **I**. (**J**) Violin plots showing the expression levels of specific genes within the Lum-D cluster. Data are split and colored by treatment for each lobe. The expression of *Krt4*, *Tacstd2*/*Trop2* and *Runx1* does not vary upon treatment, while Androgen Receptor (AR) regulated genes such as *Psca* and *Tspan1* are downregulated after castration.

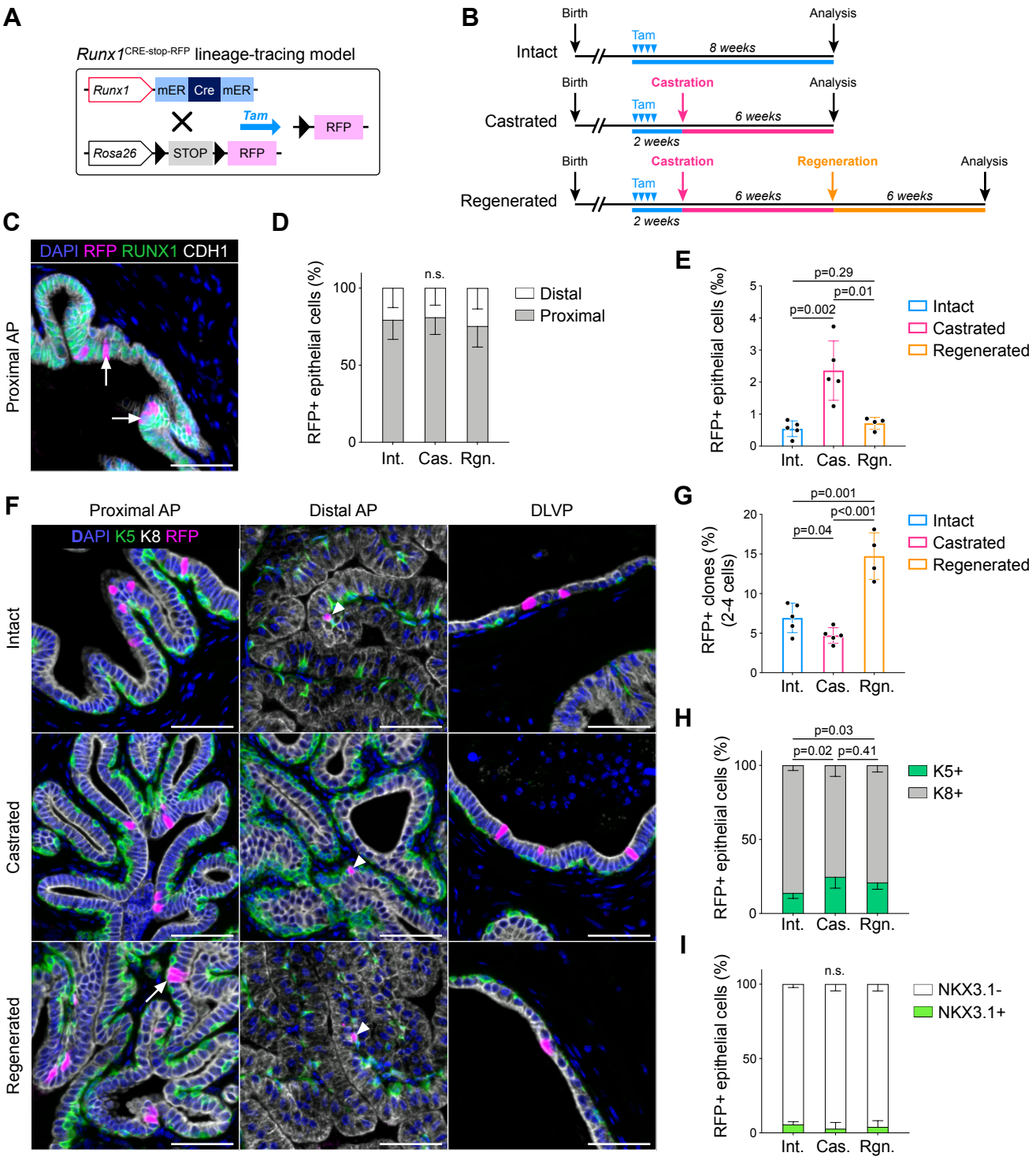

Figure 4. Lineage-tracing of *Runx1* expressing cells establishes the intrinsic castration-resistant properties of the proximal luminal lineage.

(**A**) Schematic summary of the genetic lineage tracing system employed. (**B**) Experimental strategy for lineage-tracing experiments. (**C**) Co-immunostaining of RFP, RUNX1, CDH1 in the proximal AP. Arrows indicate RFP labelled RUNX1$^+$ cells. Scale bar: 50µm. (**D**) Quantification of % of epithelial RFP$^+$ cells in proximal and distal regions of the prostate in intact (n = 5), castrated (n = 4) and regenerated (n = 4) mice. (**E**) Quantification of ‰ of epithelial RFP$^+$ cells in intact (n = 5), castrated (n = 5) and regenerated (n = 4) mice. (**F**) Co-immunostaining of RFP, K5, K8 in the proximal AP, distal AP, and DLVP (DLP + VP). Arrowheads indicate RFP labelled basal cells (K5$^+$) found in distal AP, the white arrow indicates a luminal (K8$^+$) RFP$^+$ clone made of 2 cells. Scale bar: 50µm. (**G**) Quantification of % of epithelial RFP$^+$ clones comprising between 2 to 4 cells in intact (n = 5), castrated (n = 5) and regenerated (n = 4) mice. (**H, I**) Quantification of % of RFP$^+$ cells being K5$^+$ or K8$^+$ in **H**, or NKX3.1$^+$ or NKX3.1$^-$ in **I,** in intact (n = 5), castrated (n = 5) and regenerated (n = 4) mice. Int: Intact, Cas: Castrated, Rgn: Regenerated.

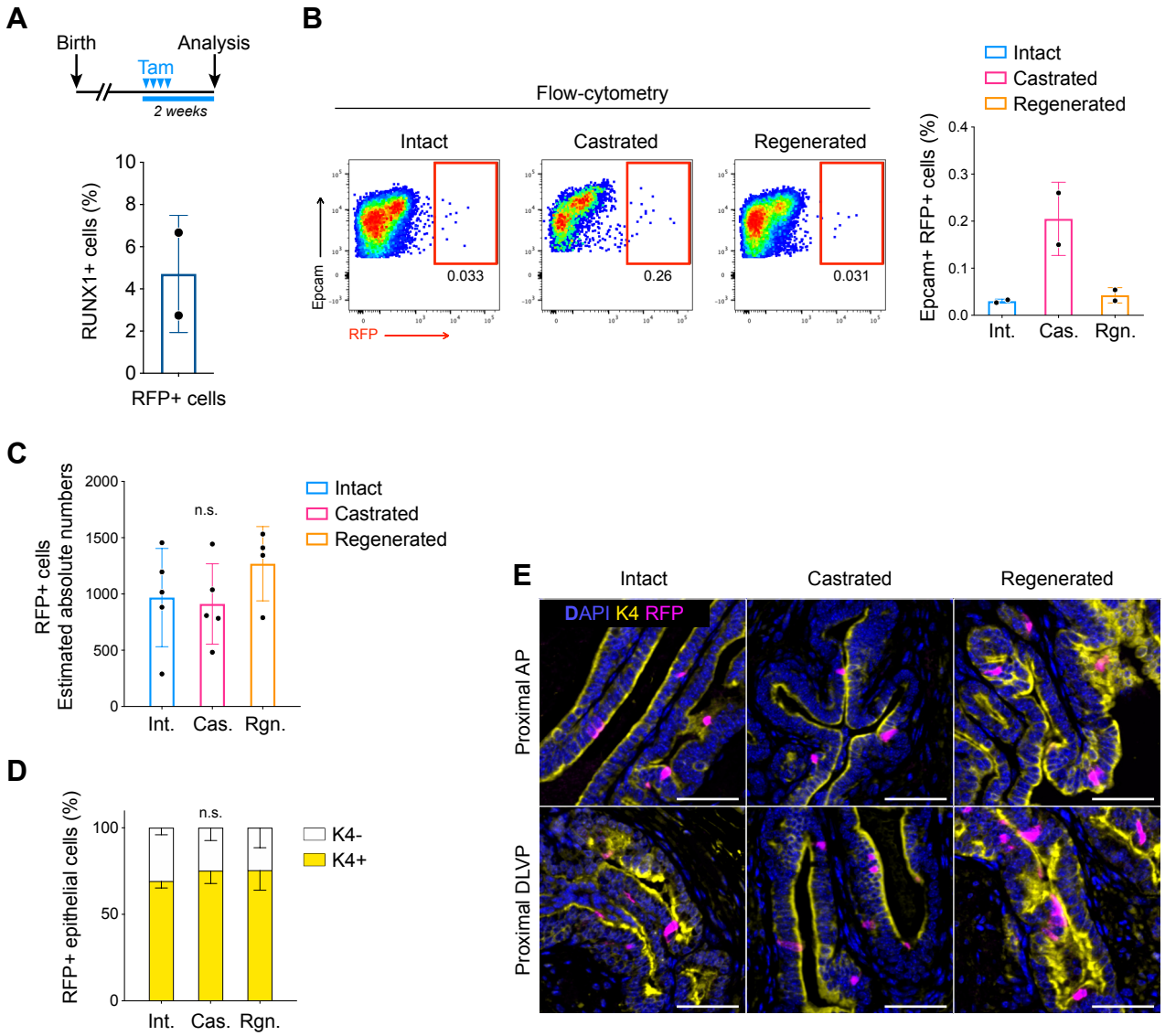

Figure 4—figure supplement 9. Lineage tracing of RUNX1 expressing cells labelled in intact mice.

(**A**) Scheme of the tamoxifen labelling strategy to evaluate the labelling efficiency of *Runx1* expressing cells. (**B**) Flow-cytometry analysis of intact (n = 2), castrated (n = 2), and regenerated (n = 2) *Runx1*$^{\text{CRE-stop-RFP}}$ mice, and corresponding quantification of the percentage of RFP$^+$ cells in the epithelial EPCAM$^+$ fraction. (**C**) Estimated absolute number of epithelial RFP$^+$ cells in intact (n = 5) and castrated (n = 5) and regenerated (n = 4) prostates based on IHC quantifications. Int: Intact, Cas: Castrated, Rgn: Regenerated. (**D**) Quantification of % of epithelial RFP$^+$ cells being K4$^+$ or K4$^-$ in intact (n = 3), castrated (n = 4) and regenerated (n = 5) mice. (**F**) Co-immunostaining showing the enrichment of K4$^+$ RFP labelled cells in the proximal region of the AP (top) and DLVP (bottom) prostate lobes. Scale bar: 50μm.

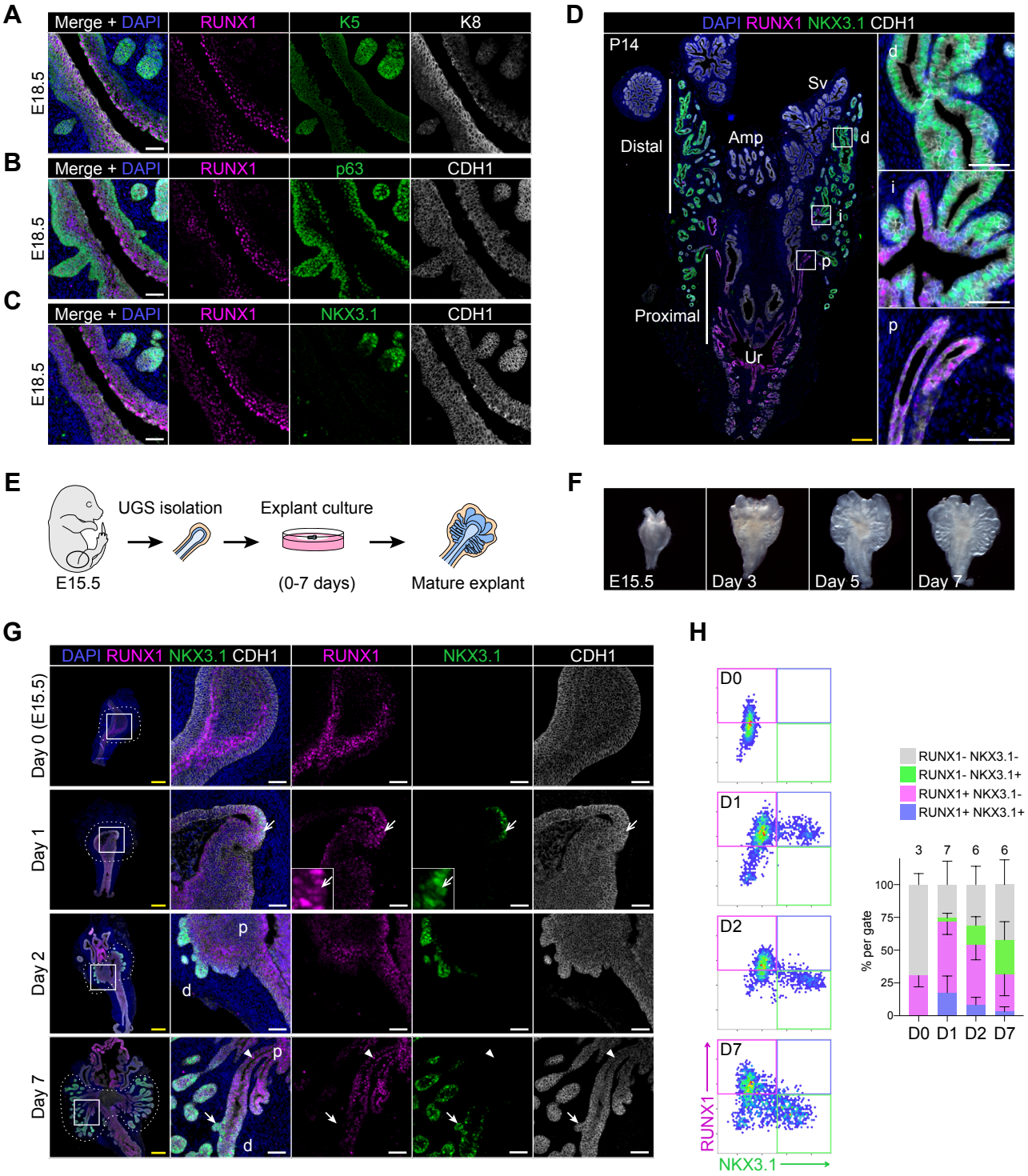

Figure 5. RUNX1 marks proximal cells during embryonic prostate development.

(**A-C**) Co-immunostainings of the mouse urogenital sinus at E18.5 for RUNX1, K5, K8 in **A**, RUNX1, p63, CDH1 in **B**, RUNX1, NKX3.1, CDH1 in **C**. Scale bar: 50µm. (**D**) Co-immunostainings of RUNX1, NKX3.1, CDH1 at postnatal (P) day 14. Higher magnification images of (p) proximal, (i) intermediate, and (d) distal regions are shown. Scale bars: 200µm (yellow) and 50µm (white). Amp: ampullary gland; Sv: seminal vesicles; Ur: urethra; p: proximal; i: intermediate; d: distal. (**E**) Scheme of the protocol to culture *ex vivo* explants of mouse UGS harvested at E15.5. (**F**) Representative images of UGS explants at E15.5 (day 0), day 3, day 5 and day 7 of culture showing the formation of premature prostate buds. (**G**) Co-immunostaining of RUNX1, NKX3.1, CDH1 in UGS explants harvested at day 0, day 1, day 2 and day 7. Higher magnification images of each square (left) are shown for each time point. Chevron arrows show RUNX1$^+$ NKX3.1$^+$ cells, closed arrows indicate RUNX1$^-$ NKX3.1$^+$ cells, arrowheads show RUNX1$^+$ NKX3.1$^-$ cells. Scale bars: 200µm (yellow) and 50µm (white). (**H**) Quantification of RUNX1 and NKX3.1 nuclear intensity (log10) in CDH1$^+$ epithelial cells of UGS explants by QBIC. Quantification was performed within the boundaries delimited in **G** by dotted lines, at day 0 (n = 3 explants), day 1 (n = 7 explants), day 2 (n = 6 explants) and day 7 (n = 6 explants).

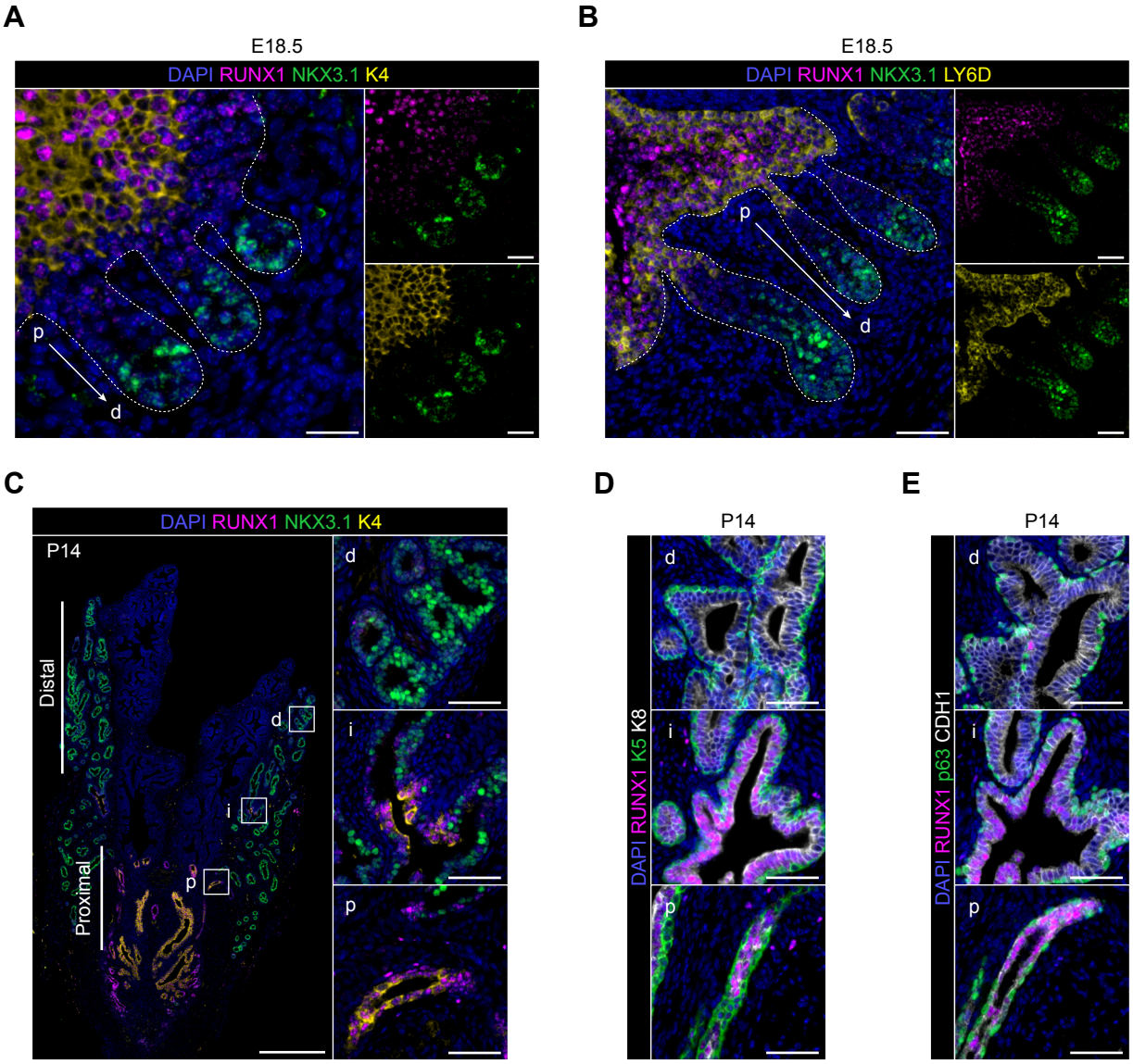

Figure 5—figure supplement 10. Characterization of RUNX1 expression during prostate development *in vivo*.

(**A**) Co-immunostainings of the mouse urogenital sinus at E18.5 for RUNX1, NKX3.1, K4. p: proximal, d: distal. Scale bar: 50μm. Dotted lines indicate the urogenital epithelium. (**B**) Co-immunostainings of the mouse urogenital sinus at E18.5 for RUNX1, NKX3.1, LY6D. p: proximal, d: distal. Scale bar: 50μm. (**C**) Co-immunostaining of RUNX1, NKX3.1, K4 at postnatal (P) day 14. Higher magnification images of (p) proximal, (i) intermediate, and (d) distal regions are shown. Scale bars: 200μm (yellow) and 50μm (white). (**D**, **E**) Co-immunostainings at postnatal P14 for RUNX1, K5, K8 in **B** RUNX1, p63, CDH1 in **C**. p: proximal, i: intermediate, d: distal. Scale bar: 50μm.

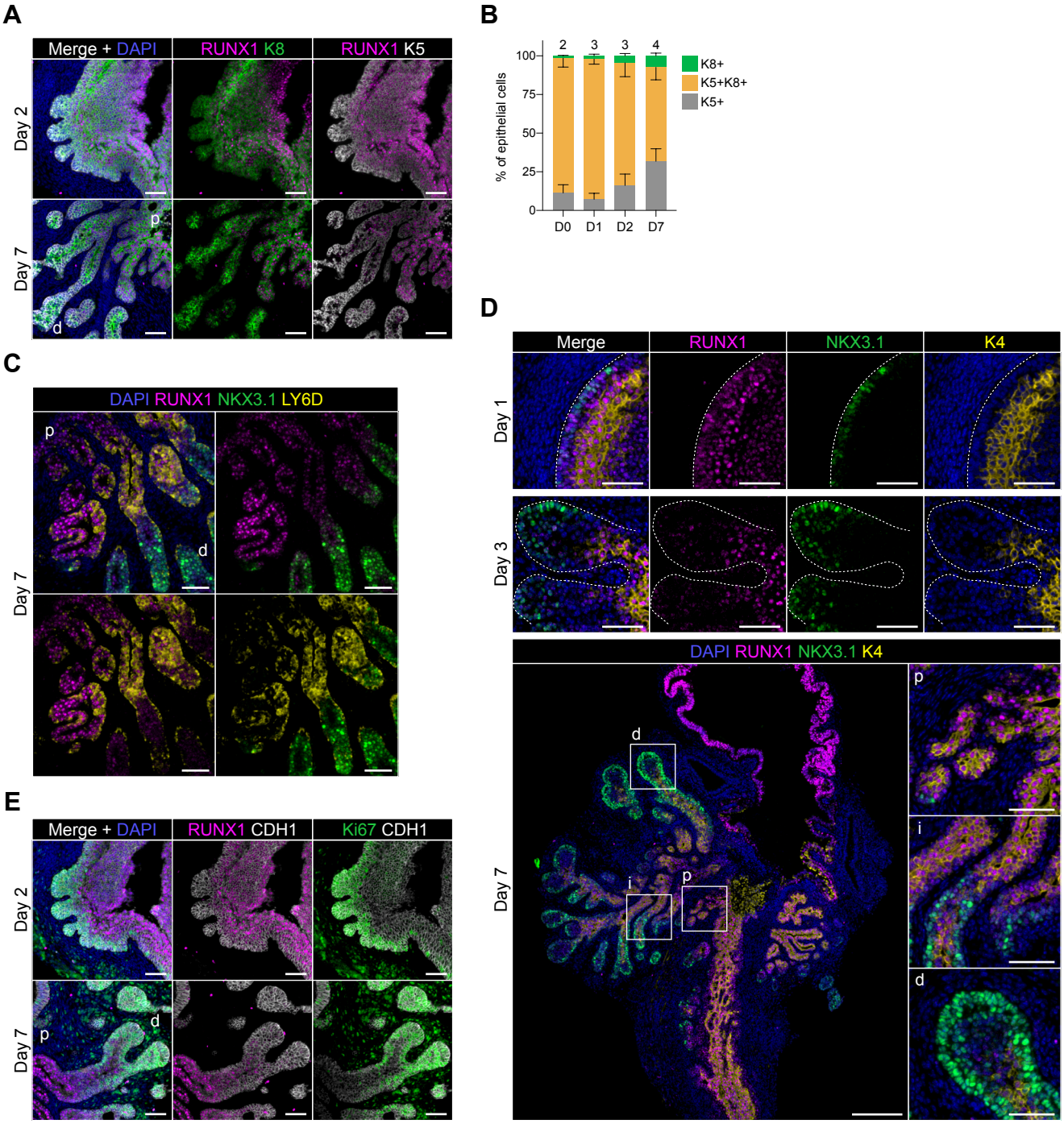

Figure 5—figure supplement 11. Characterization of RUNX1 expression during prostate development in UGS explant cultures.

(**A**) Co-immunostaining of RUNX1, K5, K8 in UGS explants harvested at day 2 and day 7. p: proximal, d: distal. Scale bar: 50μm. (**E**) Quantification of the percentage of $K5^+$, $K8^+$, $K5^+$ $K8^+$ cells during UGS explant cultures at day 0 (*n* = 2 explants), day 1 (*n* = 3 explants), day 2 (*n* = 3 explants), day 7 (*n* = 4 explants), showing a progressive reduction in the proportion of $K5^+$ $K8^+$ double positive cells. (**C**) Co-immunostaining of RUNX1, NKX3.1, LY6D in UGS explants harvested at day 7. p: proximal, d: distal. Scale bar: 50μm. (**D**) Co-immunostaining of RUNX1, NKX3.1, K4 in UGS explants harvested at day 1 (top), 3 (middle) and 7 (bottom). Higher magnification images of (p) proximal, (i) intermediate, and (d) distal regions are shown for day 7. Scale bars: 200μm (yellow) and 50μm (white). Dotted lines indicate the urogenital epithelium. (**E**) Co-immunostaining of RUNX1, Ki67, CDH1 in UGS explants harvested at day 2 and day 7. p: proximal, d: distal. Scale bar: 50μm.

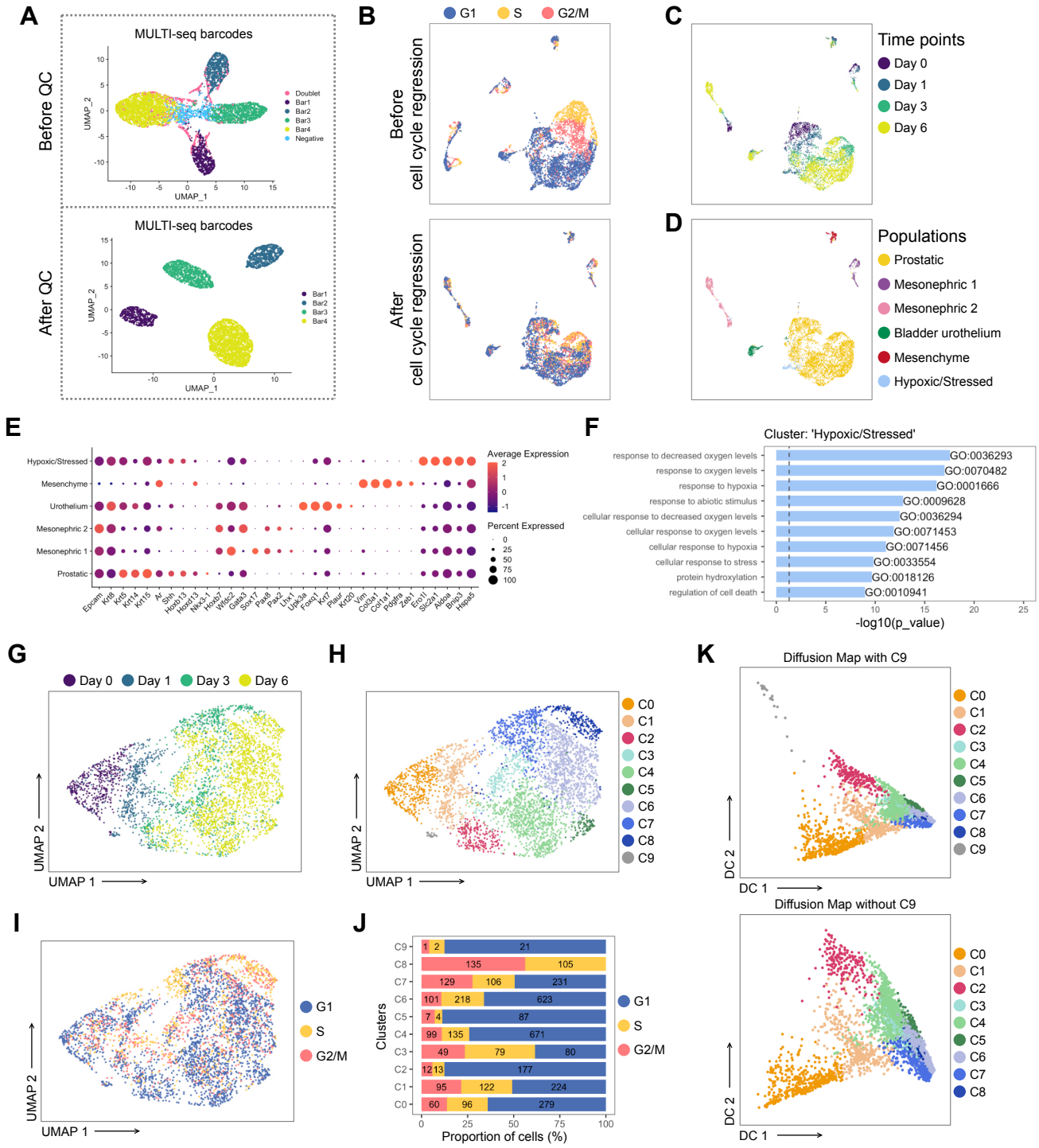

Figure 6—figure supplement 12. Pre-processing of the scRNA-seq dataset of UGS explant cultures.

(**A**) UMAP visualization in MULTI-seq barcodes space before (top) and after (bottom) quality control and barcode filtration (see Methods for details). (**B**) UMAP visualization of the dataset colored by estimated cell cycle phase (top). Due to the strong underlying impact on clustering, the cell cycle effect was regressed out (bottom). (**C, D**) UMAP visualization of the dataset colored in **C** by experimental time point and in **D** by labeled populations. (**E**) Dot plot showing the expression of selected marker genes associated with each labelled population. (**F**) Bar plots of the 10 most significantly (g:Profiler adjusted p-value < 0.05) enriched gene ontology (GO) terms (GO:BP, Biological Processes) on the differentially upregulated genes specific to the 'Hypoxic/Stressed' cluster. (**G-I**) UMAP visualization of the prostatic subset (from **D**), labelled by time points in **G**, clusters in **H**, estimated cell cycle phase in **I**. (**J**) Percentage of cells in the different estimated cell cycle phases in each clusters. (**K**) Diffusion maps representation of the prostatic subset using the first 2 diffusion components with (top) and without C9 (bottom). C9 was excluded for downstream analyses due to its outlying profile.

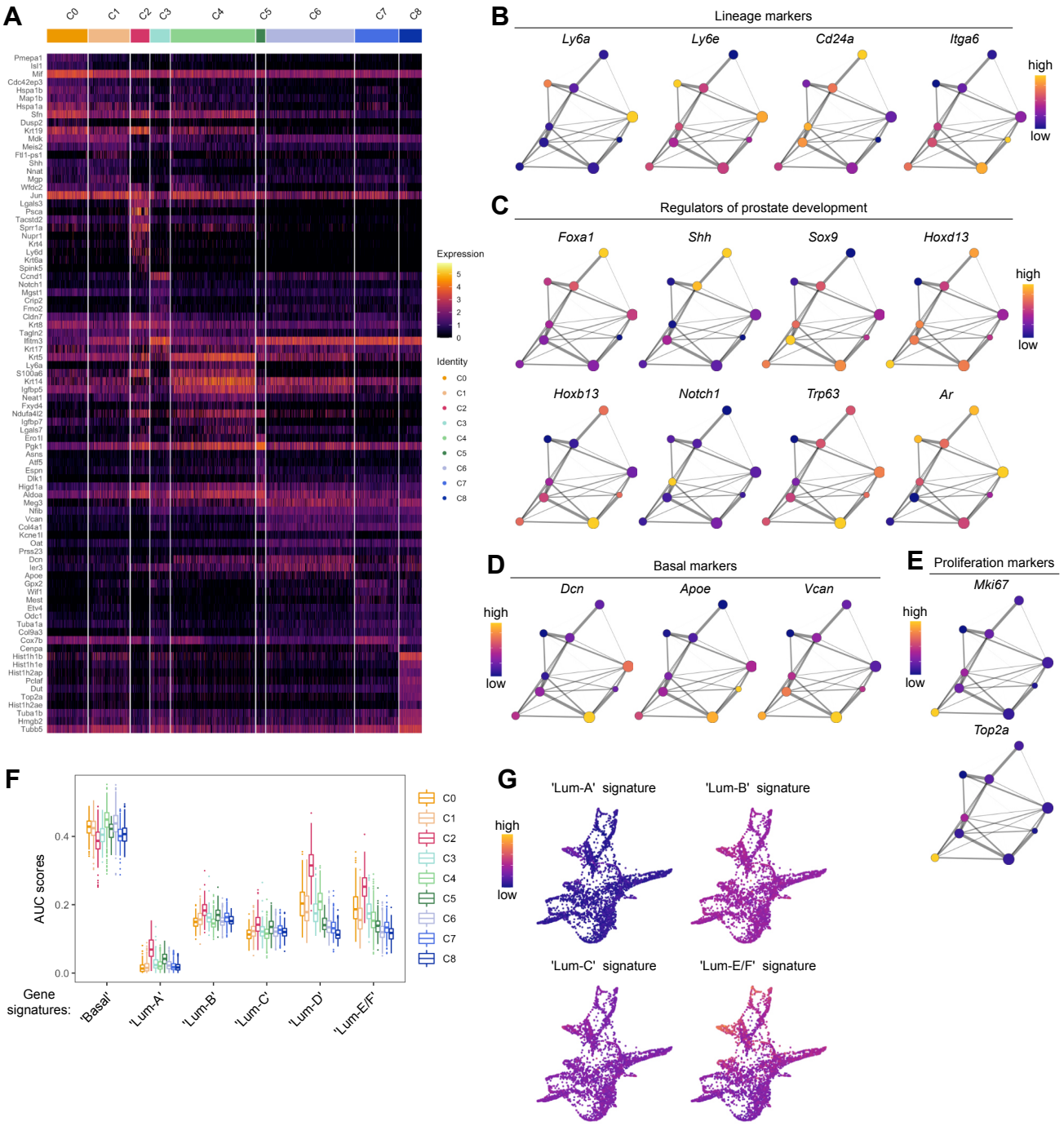

Figure 6—figure supplement 13. Characterization of the developing prostatic epithelium in the scRNA-seq dataset of UGS explant culture.

(**A**) Heatmap of the 10 most differentially upregulated genes per cluster. (**B**-**E**) PAGA representations with cluster nodes colored by a gradient representing the mean log-normalized expression levels of each genes indicated. (**B**) shows the expression of common prostate lineage markers, (**C**) shows known regulators of prostate development, (**D**) shows basal markers, (**E**) shows proliferation markers. (**F**) Box plots of per-cell AUC signature scores calculated using the 'AUCell' package for individual UGS explant clusters. Gene signatures were generated using the list of differentially upregulated genes previously obtained from our adult mouse prostate clusters. (**G**) Force directed visualization of the developing prostatic epithelium in UGS explant cultures. Color gradient represents AUC scores per cell.

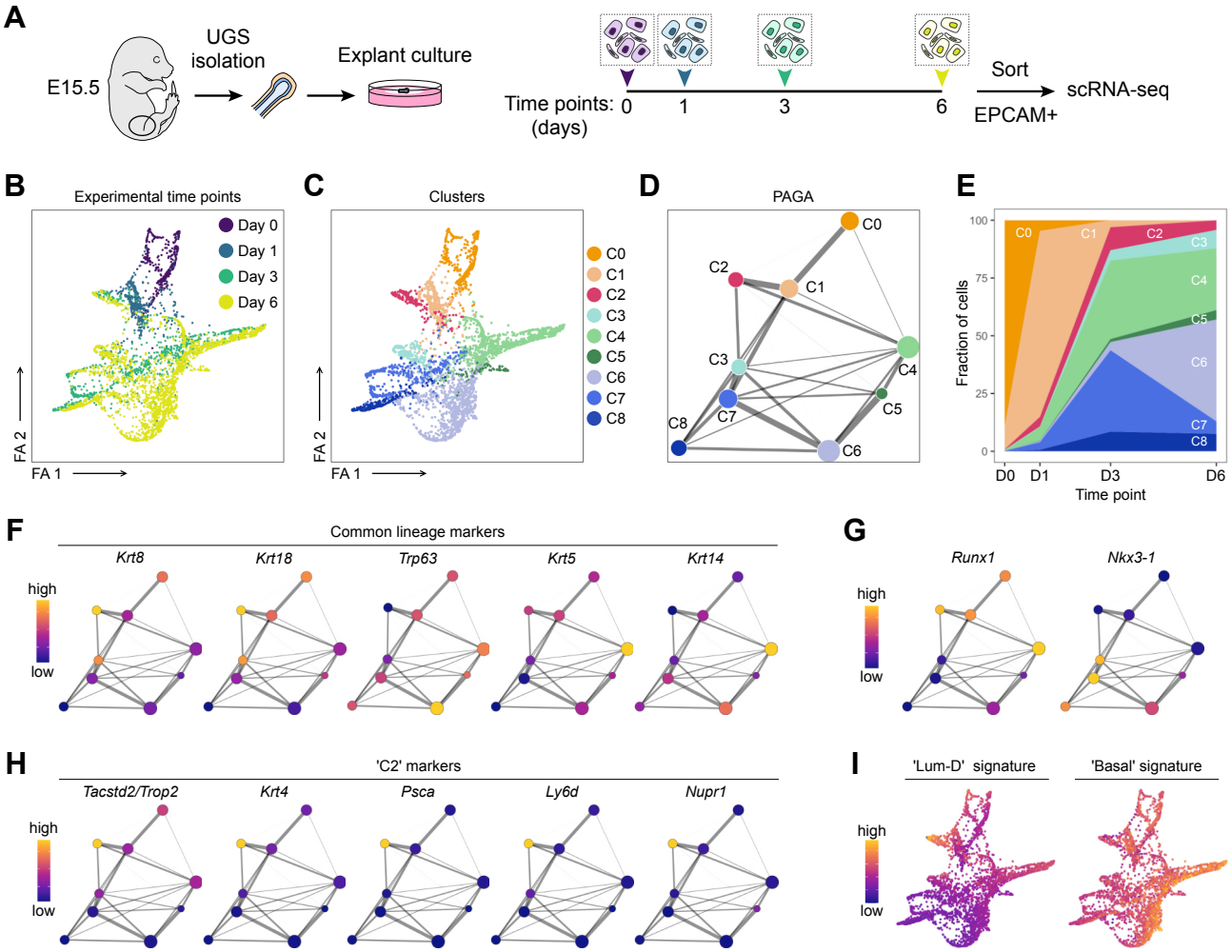

Figure 6. scRNA-seq of UGS explant cultures shows specification of the proximal luminal lineage during embryonic prostate development.

(**A**) Experimental strategy for scRNA-seq of UGS explant cultures at day 0, day 1, day 3 and day 6. (**B**, **C**) Force directed visualization of the developing prostatic epithelium in UGS explant cultures. In **B** cells are colored by experimental time points, and in **C** cells are colored by clusters. (**D**) PAGA representation of the clusters as in **C**. Weighted edges between cluster nodes represent a statistical measure of connectivity. (**E**) Fraction of cells per cluster at each experimental time point, displaying a progressive cellular diversification. (**F-H**) PAGA representations with cluster nodes colored by a gradient representing the mean log-normalized expression levels of each gene. (**I**) Force directed visualization of the developing prostatic epithelium in UGS explant cultures. Color gradient represents AUC scores per cell. Per-cell AUC scores were calculated using the 'AUCell' package. Gene signatures for 'Lum-D' (left) and 'Basal' (right) were generated using the list of differentially upregulated genes previously obtained from our adult mouse prostate clusters.

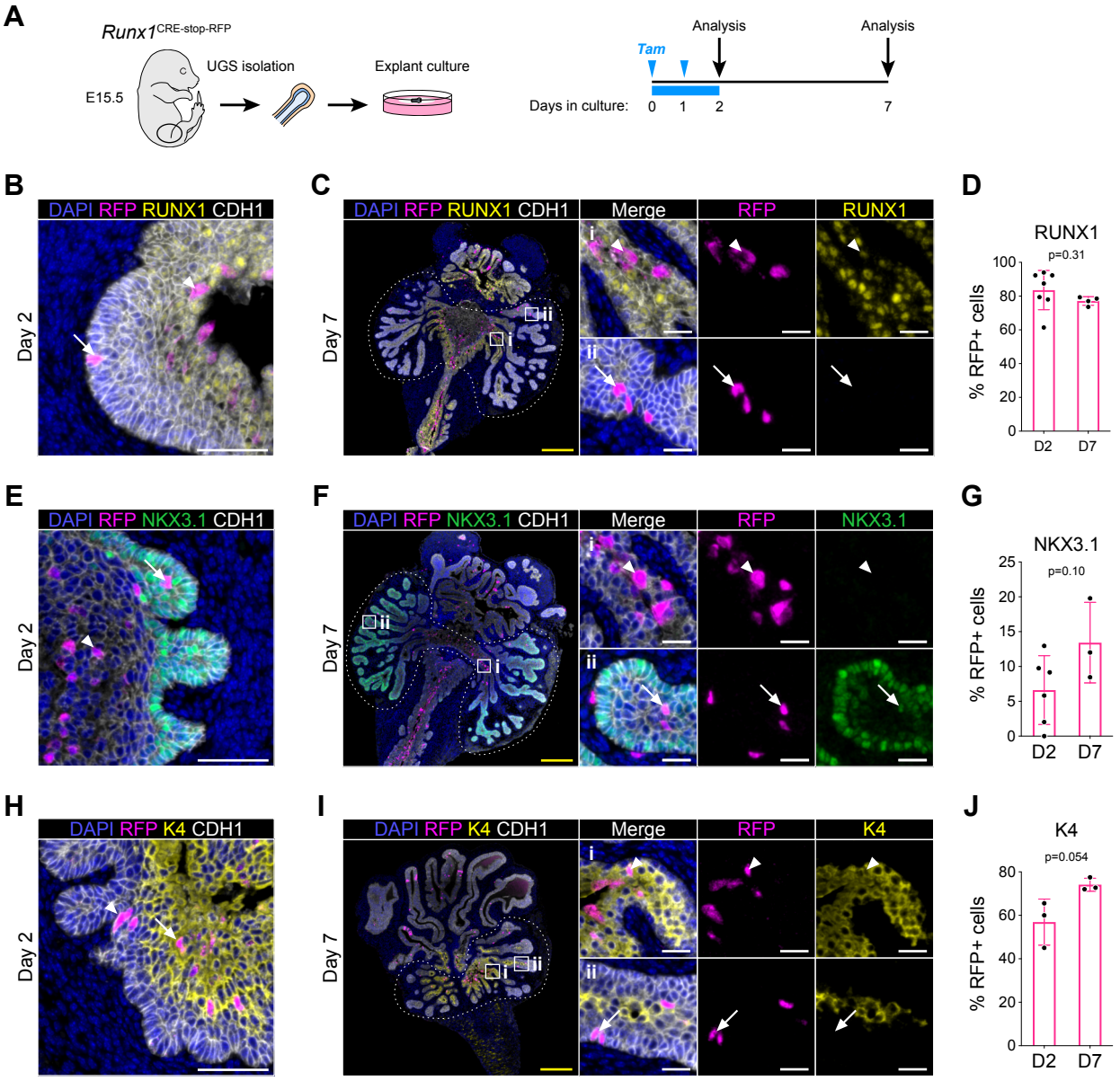

Figure 7. RUNX1⁺ cells contribute to the establishment of the proximal luminal lineage during embryonic prostate development.

(**A**) Strategy for lineage-tracing of RUNX1⁺ cells in UGS explant cultures. Tamoxifen was applied on day 0 and day 1 and washed out on day 2. (**B, C**) Co-immunostaining of RFP, RUNX1, CDH1 in UGS explants harvested at day 2 (**B**) and day 7 (**C**). Higher magnification images of proximal (i) and (ii) distal regions are shown for day 7. Arrows show RFP⁺ RUNX1-low cells, arrowheads show RFP⁺ RUNX1⁺ cells. Scale bars: 200µm (yellow) and 50µm (white). (**C**) Quantification of % of epithelial RUNX1⁺ cells in the RFP subset at day 2 (*n* = 7) and day 7 (*n* = 3) of UGS explant cultures. Quantification was performed within the boundaries delimited in **B** by dotted lines. (**E, F**) Co-immunostaining of RFP, NKX3.1, CDH1 in UGS explants harvested at day 2 (**E**) and day 7 (**F**). Higher magnification images of (i) proximal and (ii) distal regions are shown for day 7. Arrows show RFP⁺ NKX3.1⁺ cells, arrowheads show RFP⁺ NKX3.1⁻ cells. Scale bars: 200µm (yellow) and 50µm (white). (**G**) Quantification of % of epithelial NKX3.1⁺ cells in the RFP subset at day 2 (*n* = 6) and day 7 (*n* = 4) of UGS explant cultures. Quantification was performed within the boundaries delimited in **F** by dotted lines. (**H, I**) Co-immunostaining of RFP, K4, CDH1 in UGS explants harvested at day 2 (**H**) and day 7 (**I**). Higher magnification images of (i) proximal and (ii) distal regions are shown for day 7. Arrows show RFP⁺ K4⁻ cells, arrowheads show RFP⁺ K4⁺ cells. Scale bars: 200µm (yellow) and 50µm (white). (**J**) Quantification of % of epithelial K4⁺ cells in the RFP subset at day 2 (*n* = 3) and day 7 (*n* = 3) of UGS explant cultures. Quantification was performed within the boundaries delimited in **I** by dotted lines.

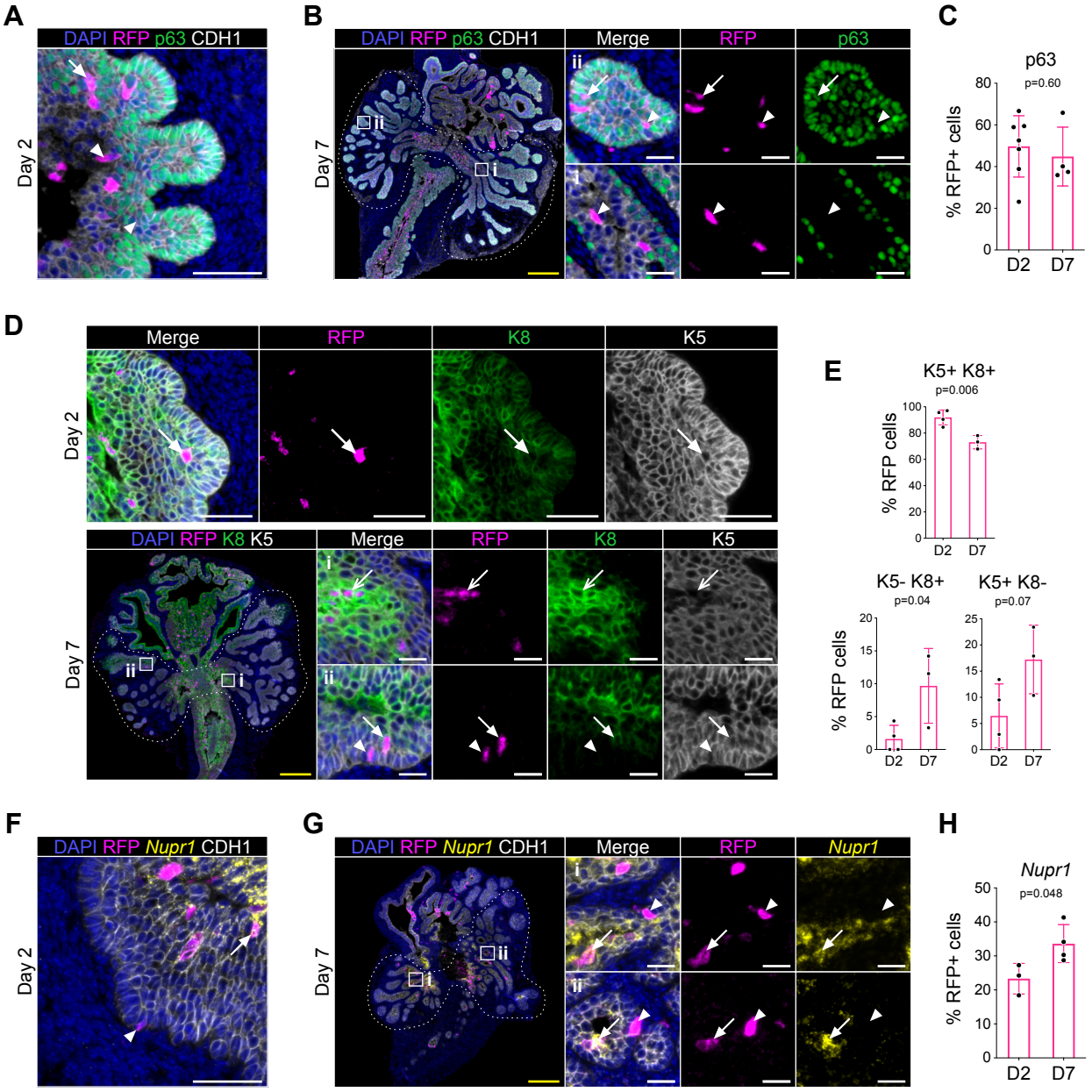

Figure 7—figure supplement 14. Lineage-tracing of RUNX1 expressing cells in UGS explants.

(**A, B**) Co-immunostaining of RFP, p63, CDH1 in UGS explants harvested at day 2 (**A**) and day 7 (**B**). Higher magnification images of (i) proximal and (ii) distal regions are shown for day 7. Arrows show RFP$^+$ p63$^+$ cells, arrowheads show RFP$^+$ p63$^-$ cells. Scale bars: 200µm (yellow) and 50µm (white). (**C**) Quantification of the percentage of epithelial RFP$^+$ p63$^+$ cells at day 2 (n = 7) and day 7 (n = 4) of UGS explant cultures. Quantification was performed within the boundaries delimited in **B** by dotted lines. (**D**) Co-immunostaining of RFP, K5, K8 in UGS explants harvested at day 2 (top) and day 7 (bottom). Higher magnification images of proximal (i) and (ii) distal regions are shown for day 7. Arrows show RFP$^+$ K5$^+$ K8$^+$ cells, chevron arrows show RFP$^+$ K5$^-$ K8$^+$, arrowheads show RFP$^+$ K5$^+$ K8$^-$ cells. Scale bars: 200µm (yellow) and 50µm (white). (**E**) Quantification of the percentage of epithelial K5$^+$ K8$^+$, K5$^-$ K8$^+$ cells and K5$^+$ K8$^-$ cells in the RFP subset at day 2 (n = 4) and day 7 (n = 3) of UGS explant cultures. Quantifications were performed within the boundaries delimited in **D** by dotted lines. (**F, G**) Co-immunostaining of RFP, *Nupr1* (mRNA), CDH1 in UGS explants harvested at day 2 (**F**) and day 7 (**G**). Higher magnification images of (i) proximal and (ii) distal regions are shown for day 7. Arrows show RFP$^+$ *Nupr1*$^+$ cells, arrowheads show RFP$^+$ *Nupr1*$^-$ cells. Scale bars: 200µm (yellow) and 50µm (white). **(J)** Quantification of % of epithelial K4$^+$ cells in the RFP subset at day 2 (n = 3) and day 7 (n = 4) of UGS explant cultures. Quantification was performed within the boundaries delimited in **G** by dotted lines.